



UNIVERSITÀ POLITECNICA DELLE MARCHE

---

FACOLTA' DI INGEGNERIA

Corso di Laurea in Ingegneria Informatica e dell'Automazione

**SINCRONIZZAZIONE DI SISTEMI NON  
LINEARI DEL SECONDO ORDINE SU  
GRUPPI DI LIE APPLICATA A  
SATELLITI E DRONI**

**SYNCHRONIZATION OF SECOND-ORDER  
NON-LINEAR SYSTEMS ON LIE-GROUPS  
APPLIED TO SATELLITES AND  
DRONES**

**Relatore:**  
**Chiar.mo Prof.**  
**SIMONE FIORI**

**Correlatore:**  
**Dr.**  
**HWEE KUAN LEE**

**Presentata da:**  
**CLAUDIO MENOTTA**

**Anno Accademico 2018/19**



# Contents

<b>1</b>	<b>Introduction</b>	<b>1</b>
<b>2</b>	<b>Dynamical systems on manifolds and Lie groups</b>	<b>3</b>
<b>3</b>	<b>Mathematical model of Hard-Duffing oscillator on Lie Group</b>	<b>6</b>
3.1	Oscillators on Lie Group . . . . .	6
3.2	Hard-Duffing oscillator . . . . .	7
<b>4</b>	<b>Mathematical model of a gyrostat satellite and of a quadcopter drone</b>	<b>9</b>
4.1	Model a gyrostat satellite on $SO(3) \times \mathfrak{so}(3)$ . . . . .	9
4.2	Mathematical model of quadrotor drone on $SO(3) \times \mathfrak{so}(3) \times \mathbb{R}^3$ .	12
<b>5</b>	<b>Numerical simulation of Hard-Duffing oscillator on the special orthogonal group <math>SO(3)</math></b>	<b>17</b>
5.1	Visual rendering via a group action on a manifold . . . . .	18
5.2	Results of numerical simulations on a hard Duffing oscillator . . .	18
<b>6</b>	<b>Numerical simulations of the gyrostat satellite and of the quadcopter drone</b>	<b>21</b>
6.1	Numerical simulation methods . . . . .	21
6.2	Results of the numerical simulation of the gyrostat satellite . . . .	22
6.3	Results of the numerical simulation of the quadcopter drone . . .	23

---

<b>7</b>	<b>Non-linear control of dynamical systems on Lie groups</b>	<b>28</b>
7.1	Proportional-integral-derivative control theory . . . . .	28
7.2	Extension of PID regulation to Lie groups (L-PID) . . . . .	29
7.2.1	Extension of PID regulation to the 3D rotation group . . . . .	32
7.3	Control efforts . . . . .	33
7.4	Application of L-PID to time-synchronization of second-order systems . . . . .	34
7.5	Application of L-PID to time-synchronization of two oscillators . . . . .	36
7.6	Application of L-PID to the time-synchronization of the attitude of two quadrotor drones . . . . .	38
7.7	Adaptation of an L-PID controller to the time-synchronization of the attitude and of the positioning of two quadrotor drones . . . . .	41
<b>8</b>	<b>Numerical experiments on the time-synchronization of oscillators, satellites and drones</b>	<b>48</b>
8.1	Synchronization of two cubes . . . . .	48
8.2	Gyrostat satellites synchronization . . . . .	53
8.3	Quadrotor drones synchronization – attitude control . . . . .	60
8.4	Quadrotor drones synchronization – mixed attitude and position control . . . . .	66
<b>9</b>	<b>Conclusion</b>	<b>70</b>

# List of Figures

4.1	Gyrostat reference frames (adapted from [10]). . . . .	10
4.2	Quadcopter reference frames. . . . .	13
5.1	Behaviour of a hard Duffing oscillator (5.2) on the special orthogonal group $SO(3)$ , in the absence of non-linear damping (namely, $\mu = 0$ ). The left-hand side panel shows the trajectory on the special orthogonal group $SO(3)$ , when the starting point and also the reference point are taken randomly, (denoted by a blue open circle) and the initial speed will be random, because related to the initial state. The parameters used in the simulation are $\kappa = 0.5$ and $h = 0.0005$ .	19
5.2	Behaviour of a hard Duffing oscillator (5.2) in the presence of non-linear damping. The left-hand panel shows the trajectory in the special orthogonal group $SO(3)$ , when the starting point and also the reference point are taken randomly (denoted by a blue open circle) the initial speed will be random, because related to the initial state. The parameters used in the simulation are $\kappa = 0.5$ , $\mu = 0.5$ , $\varepsilon = 1.3$ and $h = 0.0008$ . . . . .	20
6.1	Behaviour of a gyrostat oscillating around its contact point with the $x - y$ plane, that is the origin. In the top-left panel it can be seen the gyrostat at $k = 1,000$ , in the top-right panel at $k = 20,000$ , in the bottom-left panel with $k = 30,000$ and in the bottom-right panel with $k = 45,000$ . . . . .	23

---

6.2	Behaviour of the quadrotor drone (6.2) that performs only rotational movements, in which it oscillates around the center of mass, that is in the origin of the reference system. . . . .	24
6.3	Behaviour of a drone performing a hover maneuver. It is possible to see that the object remains parallel to the $x$ - $y$ plane thus maintaining the same height. In the top-left panel it can be seen a 3D view, while in the top-right panel there is a $x$ - $y$ view, in the bottom-left panel there is a $x$ - $z$ view and in the bottom-right panel there is a $y$ - $z$ view. . . . .	25
6.4	Behaviour of a drone performing a yaw and roll maneuver. It is possible to see that the object is turning and moving along the negative $y$ direction. . . . .	26
6.5	Behaviour of a drone performing a yaw and pitch maneuver. It is possible to see that the object is turning and moving along the positive $x$ direction. . . . .	26
6.6	Behaviour of a drone performing a pitch and roll maneuver. It is possible to see that the object is turning and moving along the positive direction of both $x$ and $y$ axes. . . . .	27
7.1	Classical PID control scheme, where $y_{sp}$ denotes the set point, $y_m$ denotes a measure of the controlled variable $y$ , $u$ denotes a control signal and $e$ denotes an error signal, which quantifies the discrepancy between the measured controlled variable and the set point. . . . .	29

8.1 Synchronization of two cubes with different reference attitudes, where the follower is controlled by a L-PID controller, without the contribution of  $U_C$ . The first four figures represent four successive instants during the process of synchronization of the two bodies. In particular the black object denotes the follower, while the red one denotes the leader. The last six figures show the kinetic, potential and total energy of the follower and leader, the behavior of the distance between the leader and follower attitude, the distance between the leader and its reference attitude and the distance between the follower and its reference attitude, and the control effort  $\sigma$ . In the attitude controller the coefficients are  $\kappa_P = 10$ ,  $\kappa_I = 5$ ,  $\kappa_D = 10$ . . . . . 50

8.2 Synchronization of two cubes with different reference attitudes, where the follower is controlled by a L-PID controller. The first four figures represent four successive instants during the process of synchronization of the two bodies. In particular the black object denotes the follower, while the red one denotes the leader. The last six figures show the kinetic, potential and total energy of the follower and leader, the behavior of the distance between the leader and follower attitude, the distance between the leader and its reference attitude and the distance between the follower and its reference attitude, and the three control efforts:  $\sigma$ ,  $\sigma_C$  and  $\sigma_{PID}$ . In the attitude controller the coefficients are  $\kappa_P = 10$ ,  $\kappa_I = 5$ ,  $\kappa_D = 10$ . . . 51

---

8.3 Synchronization of two cubes with same reference attitudes, where the follower is controlled by a L-PID controller, without the contribution of  $U_C$ . The first four figures represent four successive instants during the process of synchronization of the two bodies. In particular the black object denotes the follower, while the red one denotes the leader. The last six figures show the kinetic, potential and total energy of the follower and leader, the behavior of the distance between the leader and follower attitude, the distance between the leader and its reference attitude and the distance between the follower and its reference attitude, and the control effort  $\sigma$ . In the attitude controller the coefficients are  $\kappa_P = 10$ ,  $\kappa_I = 5$ ,  $\kappa_D = 10$ . . . . . 52

8.4 Synchronization of two gyrostatt satellites, where the follower is controlled by a L-PID controller, without the contribution of  $U_C$ . The first four figures represent four successive instants during the process of synchronization of the two bodies. In particular the black object denotes the follower, while the red one denotes the leader. The last two figures show the behavior of the distance between the leader and follower attitude and the control effort  $\sigma$ . The proportional control coefficient was set to  $\kappa_P = 10$ , the integral control coefficient was set to  $\kappa_I = 5$  and the derivative coefficient was set to  $\kappa_D = 10$ . . . . . 54

- 8.5 Synchronization of two gyrostat satellites, where the follower is controlled by a L-PID controller and the PID is made by only the proportional part (P). The first figure represents the last instant of the process of synchronization of the two bodies. In particular the black object denotes the follower, while the red one denotes the leader. The last two figures show the behavior of the distance between the leader and follower attitude and the three control efforts:  $\sigma$ ,  $\sigma_C$  and  $\sigma_P$ . The proportional control coefficient was set to  $\kappa_P = 10$ , the integral control coefficient was set to  $\kappa_I = 0$  and the derivative coefficient was set to  $\kappa_D = 0$ . . . . . 55
- 8.6 Synchronization of two gyrostat satellites, where the follower is controlled by a L-PID controller and the PID is made by only the integral and derivative parts (ID). The first figure represents the last instant of the process of synchronization of the two bodies. In particular the black object denotes the follower, while the red one denotes the leader. The last two figures show the behavior of the distance between the leader and follower attitude and the three control efforts:  $\sigma$ ,  $\sigma_C$  and  $\sigma_{ID}$ . The proportional control coefficient was set to  $\kappa_P = 0$ , the integral control coefficient was set to  $\kappa_I = 5$  and the derivative coefficient was set to  $\kappa_D = 10$ . . . . . 56
- 8.7 Synchronization of two gyrostat satellites, where the follower is controlled by a L-PID controller and the PID is made by only proportional and integral parts (PI). The first four figures represent four successive instants during the process of synchronization of the two bodies. In particular the black object denotes the follower, while the red one denotes the leader. The last two figures show the behavior of the distance between the leader and follower attitude and the three control efforts:  $\sigma$ ,  $\sigma_C$  and  $\sigma_{PI}$ . The proportional control coefficient was set to  $\kappa_P = 10$ , the integral control coefficient was set to  $\kappa_I = 5$  and the derivative coefficient was set to  $\kappa_D = 0$ . 57

---

8.8	Synchronization of two gyrostat satellites, where the follower is controlled by a L-PID controller and the PID is made by only proportional and derivative parts (PD). The first four figures represent four successive instants during the process of synchronization of the two bodies. In particular the black object denotes the follower, while the red one denotes the leader. The last two figures show the behavior of the distance between the leader and follower attitude and the three control efforts: $\sigma$ , $\sigma_C$ and $\sigma_{PD}$ . The proportional control coefficient was set to $\kappa_P = 10$ , the integral control coefficient was set to $\kappa_I = 0$ and the derivative coefficient was set to $\kappa_D = 10$ .	58
8.9	Synchronization of two gyrostat satellites, where the follower is controlled by a L-PID controller. The first four figures represent four successive instants during the process of synchronization of the two bodies. In particular the black object denotes the follower, while the red one denotes the leader. The last two figures show the behavior of the distance between the leader and follower attitude and the three control efforts: $\sigma$ , $\sigma_C$ and $\sigma_{PID}$ . The proportional control coefficient was set to $\kappa_P = 10$ , the integral control coefficient was set to $\kappa_I = 5$ and the derivative coefficient was set to $\kappa_D = 10$ .	59
8.10	Synchronization of two drones, where the follower is controlled by a L-PID controller, without the contribution of $U_C$ . The first four figures represent four successive instants during the process of synchronization of the two bodies. In particular the blue object denotes the follower, while the red one denotes the leader. The last two figures show the behavior of the distance between the leader and follower attitude and the control effort $\sigma$ . The proportional control coefficient was set to $\kappa_P = 10$ , the integral control coefficient was set to $\kappa_I = 5$ and the derivative coefficient was set to $\kappa_D = 10$ .	61

- 8.11 Synchronization of two drones, where the follower is controlled by a L-PID controller and the PID is made by only the proportional part (P). The first figure represents the last instant of the process of synchronization of the two bodies. In particular the blue object denotes the follower, while the red one denotes the leader. The last two figures show the behavior of the distance between the leader and follower attitude and the three control efforts:  $\sigma$ ,  $\sigma_C$  and  $\sigma_P$ . The proportional control coefficient was set to  $\kappa_P = 10$ , the integral control coefficient was set to  $\kappa_I = 0$  and the derivative coefficient was set to  $\kappa_D = 0$ . . . . . 62
- 8.12 Synchronization of two drones, where the follower is controlled by a L-PID controller and the PID is made by only the integral and derivative parts (ID). The first figure represents the last instant of the process of synchronization of the two bodies. In particular the blue object denotes the follower, while the red one denotes the leader. The last two figures show the behavior of the distance between the leader and follower attitude and the three control efforts:  $\sigma$ ,  $\sigma_C$  and  $\sigma_{ID}$ . The proportional control coefficient was set to  $\kappa_P = 0$ , the integral control coefficient was set to  $\kappa_I = 5$  and the derivative coefficient was set to  $\kappa_D = 10$ . . . . . 62
- 8.13 Synchronization of two drones, where the follower is controlled by a L-PID controller and the PID is made by only proportional and integral parts (PI). The first four figures represent four successive instants during the process of synchronization of the two bodies. In particular the blue object denotes the follower, while the red one denotes the leader. The last two figures show the behavior of the distance between the leader and follower attitude and the three control efforts:  $\sigma$ ,  $\sigma_C$  and  $\sigma_{PI}$ . The proportional control coefficient was set to  $\kappa_P = 10$ , the integral control coefficient was set to  $\kappa_I = 5$  and the derivative coefficient was set to  $\kappa_D = 0$ . . . . . 64

---

8.14 Synchronization of two drones, where the follower is controlled by a L-PID controller. The first four figures represent four successive instants during the process of synchronization of the two bodies. In particular the blue object denotes the follower, while the red one denotes the leader. The last two figures show the behavior of the distance between the leader and follower attitude and the three control efforts:  $\sigma$ ,  $\sigma_C$  and  $\sigma_{PID}$ . The proportional control coefficient was set to  $\kappa_P = 10$ , the integral control coefficient was set to  $\kappa_I = 5$  and the derivative coefficient was set to  $\kappa_D = 10$ . . . . . 65

8.15 Synchronization of two drones, where the follower is controlled by a mixed attitude and position controller. The first four figures represent four successive instants during the process of synchronization of the two bodies. In particular the blue object denotes the follower, while the red one denotes the leader. The last four figures show the behavior of the distance between the leader and follower attitude, the distance between the leader and follower position, and the three control efforts of both control signal (position and attitude):  $\sigma$ ,  $\sigma_C$  and  $\sigma_{PID}$ . In the position controller the coefficients are  $\kappa_P = 100$ ,  $\kappa_I = 10$ ,  $\kappa_D = 80$ , while in the attitude controller the coefficients are  $\kappa_P = 50$ ,  $\kappa_I = 10$ ,  $\kappa_D = 50$ . . . . . 67

8.16 Synchronization of two drones, where the follower is controlled by mixed attitude and position controller and the leader performs three different maneuvers over the time. The first four figures represent four successive instants during the process of synchronization of the two bodies. In particular the blue object denotes the follower, while the red one denotes the leader. The last four figures show the behavior of the distance between the leader and follower attitude, the distance between the leader and follower position, and the three control efforts of both control signal (position and attitude):  $\sigma$ ,  $\sigma_C$  and  $\sigma_{PID}$ . In the position controller the coefficients are  $\kappa_P = 100$ ,  $\kappa_I = 10$ ,  $\kappa_D = 80$ , while in the attitude controller the coefficients are  $\kappa_P = 50$ ,  $\kappa_I = 10$ ,  $\kappa_D = 50$ . . . . . 69

# List of Tables

4.1	Summary of four numerical experiments design, adapted from [3].	16
-----	---	----

## **Sommario**

Lo scopo principale di questo documento è presentare e testare numericamente una teoria di controllo non lineare sui gruppi di Lie ispirata al controllo proporzionale-integrale-derivativo (PID). Questo documento delinea due sistemi dinamici reali sui gruppi di Lie (un satellite girostatico e un drone a quattro eliche) e le tecniche numeriche utilizzate per implementare questi sistemi e il regolatore PID su una piattaforma di calcolo.

## **Abstract**

The main purpose of this document is to present and test numerically a non-linear control theory on Lie groups inspired by the proportional-integral-derivative (PID) regulation. This document outlines two real-world dynamical system on Lie groups (a gyrostat satellite and a quadrotor drone) and the numerical techniques used to implement these systems on a computing platform as well as to implement the PID regulator.

# 1. Introduction

Rotational dynamical systems are prototypical in Lie-group-system theory [10]. These second-order systems are described by differential equations formulated on trivialized tangent bundles, which play the role of phase-spaces for the dynamical systems. A further illustrative instance of Lie-group-based dynamical systems are those that evolve on the space of symmetric, positive-definite matrices, which are able to model human motion across video frames [20]. Regulating dynamical systems on Lie groups is a challenging and exciting research topic.

Classical proportional-integral-derivative (PID) regulators react to the regulated system's present, past and predicted future behavior [12]. Second-order non-linear systems whose states belong to curved spaces and associated tangent bundles, need special control design, which do not necessarily follow the classical rules known from the scientific literature. One of the main purposes of the present research endeavour is to design a specific PID-like control theory that is able to cope with Lie-group-type dynamical systems (L-PID), with special emphasis to synchronization of rotational dynamics.

Time-synchronization denotes the attitude of two or more systems – either identical or different – to harmonize their dynamics over time, either spontaneously or forcibly [14, 18, 22]. Time-synchronization is closely related to consensus in a network of locally-interacting agents [8, 21]. In the present research, I treat synchronization as a goal to be achieved by non-linear PID-type control and adapt a general L-PID regulation scheme to harmonizing the rotational dynamics of satellite gyrostats and of quadrotor drones. The physical feasibility of the obtained

---

control strategy and related control effort magnitude will also be discussed through numerical experiments.

To implement non-linear dynamical systems on Lie groups and the devised control strategy on a computing platform, it is necessary to develop adequate numerical methods to approximate the trajectories generated by these dynamical systems and to compute the values of the control fields. Classical numerical methods, such as the Euler method or the Runge-Kutta class, will fail if applied directly, as they were designed for flat spaces. These numerical methods may, however, be extended so as to cope with curved state manifolds by means of numerical calculus on manifold and Lie groups [6, 7].

The present document is organized as follows. Section 2 recalls some notation from manifold calculus and describes a general second-order dynamical system on Lie groups. Section 3 summarizes a mathematical models of a *Hard-Duffing oscillator*. Section 4 summarizes a mathematical models of a *gyrostat satellite* and a mathematical model of a *quadrotor drone*. Section 5 describes the numerical method used to implement the models of Hard Duffing oscillator on the group of 3D rotations. Section 6 describes the numerical method used to implement the models of a gyrostat satellite and of a quadcopter drone and shows the results of numerical simulations to illustrate the behavior of these models. Section 7 recalls the classical proportional-integral-derivative control theory for second-order dynamical systems and presents an extension of such theory to Lie groups (L-PID). In addition, the Section 7 illustrates an application of the proposed L-PID control theory to the time-synchronization of the motion of a oscillator, gyrostat satellite and of a quadcopter drone. Section 8 illustrates the L-PID-based synchronization of second-order dynamical systems taking as cases of study the Hard-Duffing oscillator, used as 'Toy Problem' to implement real systems, satellite and the quadcopter. Section 9 concludes the document.

## 2. Dynamical systems on manifolds and Lie groups

The present section recalls some notation from manifold calculus and describes a prototypical dynamical system on Lie groups. Let  $\mathbb{M}$  denote a Riemannian manifold. At a point  $x \in \mathbb{M}$ , the tangent space to the manifold  $\mathbb{M}$  is denoted as  $T_x\mathbb{M}$ . The symbol  $T\mathbb{M}$  denotes the tangent bundle defined as  $T\mathbb{M} := \{(x, v) \mid x \in \mathbb{M}, v \in T_x\mathbb{M}\}$ .

A Riemannian manifold  $\mathbb{M}$  is endowed with a bilinear, positive-definite form  $\langle \bullet, \bullet \rangle_x : T_x\mathbb{M} \times T_x\mathbb{M} \rightarrow \mathbb{R}$ . A local metric  $\langle \cdot, \cdot \rangle_x$  also defines a local norm  $\|v\|_x := \sqrt{\langle v, v \rangle_x}$ , for  $v \in T_x\mathbb{M}$ .

A *manifold exponential* map  $\exp : T\mathbb{M} \rightarrow \mathbb{M}$  applies as  $\exp_x(v)$ . Its inverse ‘log’ is defined only locally and is termed *manifold logarithm*. Given points  $x, y \in \mathbb{M}$ , a manifold logarithm computes a tangent vector  $v = \log_x(y) \in T_x\mathbb{M}$  such that  $\exp_x(v) = y$ . Given two points  $x, y \in M$  connectable by a geodesic arc, their *Riemannian* distance is denoted by  $d(x, y)$ . On a Riemannian manifold, the distance between two nearby points may be evaluated by  $d(x, y) = \sqrt{\langle \log_x(y), \log_x(y) \rangle_x}$ .

The *kinetic energy function*  $\mathcal{K} : T\mathbb{M} \rightarrow \mathbb{R}$  for a dynamical system is defined by  $\mathcal{K} := \frac{1}{2} \langle v, v \rangle_x$  for  $(x, v) \in T\mathbb{M}$ . On a Riemannian manifold, the metric is positive-definite, hence, on every trajectory, it holds that  $\mathcal{K} \geq 0$ .

A special case of manifold is a Lie group, that is a manifold which carries over additional structure, which will be denoted as  $\mathbb{G}$  in the following. A Lie group is a smooth manifold that possesses the additional structure of an algebraic group, namely, multiplication, an identity element with respect to the multiplication, and inversion  $(\bullet)^{-1}$ . The tangent space at identity, which plays a central role in Lie

---

group theory, is denoted by  $\mathfrak{g}$  and is referred to as *Lie algebra*. Given an element  $X \in \mathbb{G}$ , it is customary to define an operation  $X \cdot$  as *inverse left translation*, which maps a tangent vector from the algebra  $\mathfrak{g}$  to the tangent space  $T_X \mathbb{G}$ . By way of inverse left translation, the tangent bundle  $T\mathbb{G}$  may be trivialized to  $\mathbb{G} \times \mathfrak{g}$ , because every tangent space  $T_X \mathbb{G}$  is isomorphic to  $\mathfrak{g}$ , in fact  $T_X \mathbb{G} = X \cdot \mathfrak{g}$ .

The inner product on the Lie algebra is denoted by  $\langle \bullet, \bullet \rangle_{\mathfrak{g}}$ . Thanks to the trivialization of the tangent bundle induced by left translation, it is convenient to define the inner product  $\langle \bullet, \bullet \rangle_X$ , for  $X \in \mathbb{G}$  as  $\langle V, W \rangle_X := \langle X^{-1} \cdot V, X^{-1} \cdot W \rangle_{\mathfrak{g}}$  (where  $X^{-1} \cdot$  denotes left translation). On a Lie group it holds that

$$\text{grad}_X d^2(X, Y) = -2 \log_X Y, \quad (2.1)$$

for  $X, Y \in \mathbb{G}$  sufficiently close for their logarithm to be defined.

A general second-order dynamical system on a Lie group  $\mathbb{G}$  reads [5, 6]:

$$\begin{cases} \dot{V} = \mathbb{S}(t, X, V), & \text{(Velocity-transition equation)} \\ \dot{X} = X \cdot V, & \text{(Position-transition equation)} \end{cases} \quad (2.2)$$

in the trivialized tangent bundle variables  $(X(t), V(t)) \in \mathbb{G} \times \mathfrak{g}$ , where  $t \geq 0$ . Here, the state-transition function  $\mathbb{S}$  may be assimilated to a mechanical torque, which may be composed as the sum of several contributions, roughly classified as:

- **Internal contributions:** These contributions take into account the basic inertial phenomena, namely the mechanical torque derived by the attitude of a system to keep in motion irrespective of external solicitations as well as friction inherent to motion.
- **External contributions:** These contributions represent the action of internal as well as external solicitations (such as the action of external propellers in gyrostat satellites and of rotors in drones), that a control system may gain access to.

In applied sciences and engineering, Lie groups of interest are essentially *matrix Lie groups*, as the group of 3D rotations  $\text{SO}(3) := \{R \in \mathbb{R}^{3 \times 3} \mid R^T R = I_3, \det(R) =$

1}, where the superscript  $\top$  denotes matrix transpose. The Lie algebra associated to such Lie group is  $\mathfrak{so}(3) := \{\Omega \in \mathbb{R}^{3 \times 3} \mid \Omega^\top + \Omega = 0_3\}$ . The canonical metric for the Lie algebra  $\mathfrak{so}(3)$  reads  $\langle \Omega, \Psi \rangle_{\mathfrak{so}(3)} := \text{tr}(\Omega^\top \Psi)$ , where ‘tr’ denotes matrix trace. It is convenient to define a basis of the vector space  $\mathfrak{so}(3)$  of the skew-symmetric matrices in as  $\mathfrak{so}(3) = \text{span}(\Omega_x, \Omega_y, \Omega_z)$ , where

$$\Omega_x := \begin{bmatrix} 0 & 0 & 0 \\ 0 & 0 & -1 \\ 0 & 1 & 0 \end{bmatrix}, \quad \Omega_y := \begin{bmatrix} 0 & 0 & 1 \\ 0 & 0 & 0 \\ -1 & 0 & 0 \end{bmatrix}, \quad \Omega_z := \begin{bmatrix} 0 & -1 & 0 \\ 1 & 0 & 0 \\ 0 & 0 & 0 \end{bmatrix}. \quad (2.3)$$

The Lie algebra  $\mathfrak{so}(3)$  is endowed with two ‘brackets’: the commutator  $[\Omega, \Psi] := \Omega\Psi - \Psi\Omega$  and the anti-commutator  $\{\Omega, \Psi\} := \Omega\Psi + \Psi\Omega$ .

The exponential map and the principal logarithmic map, in this case of interest, read:

$$\begin{cases} \exp_R(V) := R\text{Exp}(R^\top V), \\ \log_R(Q) := R\text{Log}(R^\top Q), \end{cases} \quad (2.4)$$

where ‘Exp’ denotes a matrix exponential, Log denotes a matrix logarithm,  $R, Q \in \text{SO}(3)$  and  $V \in T_R\text{SO}(3)$ . The computation of the matrix logarithm is a sensitive problem and specific numerical recipes need to be invoked at times. I accessed the method described in [17].

# 3. Mathematical model of Hard-Duffing oscillator on Lie Group

The present section summarizes the mathematical model of a dynamical system, in particular the Hard-Duffing oscillator, on Lie Group. This oscillator will be used as a 'Toy Problem', first for the implementation of real dynamical systems on the Lie Group, as a gyrostat satellite and drone (sections 4 and 6), and then for the application of a PID controller developed on the Lie Group, which will also be applied later to this real systems (section 7 and 8).

## 3.1 Oscillators on Lie Group

The *kinetic energy function*  $\mathcal{K} : T\mathbb{M} \rightarrow \mathbb{R}$  for a dynamical system is defined by  $\mathcal{K} := \frac{1}{2} \langle v, v \rangle_x$  for  $(x, v) \in T\mathbb{M}$ . On a Riemannian manifold, the metric is positive-definite, hence, on every trajectory, it holds that  $\mathcal{K} \geq 0$ .

A *potential energy function*  $\mathcal{V} : \mathbb{M} \rightarrow \mathbb{R}$  depends on the coordinate  $x \in \mathbb{M}$  only. In absence of any external solicitation, the dynamical system generates a trajectory  $x = x(t)$  that follows the landscape of the potential energy function.

The total energy  $\mathcal{H}$  of a dynamical system is defined by:

$$\mathcal{H} := \mathcal{K} + \mathcal{V}. \tag{3.1}$$

Considering the system (2.2), in the case that it is a general oscillator on Lie Group,  $\mathbb{S}$  denotes again a forcing term (more like a mechanical torque, indeed),

which may be composed as the sum of several contributions, like:

- *Friction-type damping (dissipative force)*: This kind of damping is expressed by the forcing term  $-\mu\|V\|^{2(\varepsilon-1)}V$ . Here,  $\|\cdot\|$  denotes a norm in the Lie algebra  $\mathfrak{g}$ .
- *Conservative force*: It derives from a potential  $\mathcal{V}$  and reads  $-X^{-1} \cdot \text{grad}_X \mathcal{V}$ . The notation  $X^{-1} \cdot$  is a short-hand for left translation, which maps a tangent vector from the tangent space  $T_X \mathbb{G}$  to the algebra  $\mathfrak{g}$ .

In the following, we shall only consider the two terms above, thus the dynamical system (2.2) assumes the expression:

$$\begin{cases} \dot{X} &= X \cdot V, \\ \dot{V} &= -\mu\|V\|^{2(\varepsilon-1)}V - X^{-1} \cdot \text{grad}_X \mathcal{V}. \end{cases} \quad (3.2)$$

For more details, see [5, 6].

### 3.2 Hard-Duffing oscillator

The Hard-Duffing oscillator, named after Georg Duffing, is a non-linear second-order differential equation used to model the motion of a damped oscillator with a more complex potential than in simple harmonic motion [11]. In physical terms, it models, for example, a spring pendulum whose spring's stiffness does not exactly obey Hooke's law. An extension of the Hard-Duffing potential reads:

$$\mathcal{V}^{(\text{H-duf})} := \frac{1}{2}d^2(X, R) + \frac{1}{4}\kappa d^4(X, R), \quad (3.3)$$

where again  $d(\cdot, \cdot)$  denotes the Riemannian (geodesic) distance on the Lie Group  $\mathbb{G}$ ,  $\kappa > 0$  is a free parameter and  $R \in \mathbb{G}$  denotes a reference point. The Duffing potential is  $\mathcal{V}^{(\text{H-duf})} \geq 0$ , for any value of  $X \in \mathbb{G}$ . So the point  $X = R$  is the only point where the potential vanishes to zero and the only point of stationarity of the potential.

The Riemannian gradient of Hard-Duffing potential reads:

$$\text{grad}_X \mathcal{V}^{(\text{H-duf})} = [-1 - \kappa d^2(X, R)] \log_X(R). \quad (3.4)$$

---

Therefore, the dynamical system associated to a Duffing potential reads:

$$\begin{cases} \dot{X} &= XV, \\ \dot{V} &= -\mu \|V\|^{2(\varepsilon-1)}V + X^{-1}[1 + \kappa d^2(X, R)] \log_X(R). \end{cases} \quad (3.5)$$

## 4. Mathematical model of a gyrostat satellite and of a quadcopter drone

The present section summarizes a mathematical models of a *gyrostat satellite* and of a *quadrotor drone* within the framework of Lie-group system theory.

### 4.1 Model a gyrostat satellite on $SO(3) \times \mathfrak{so}(3)$

The gyrostats are scientific models or instruments designed to illustrate experimentally the dynamics of a rotating body such as the spinning-top, the hoop and the bicycle, and also the precession of the equinox and the rotation of the earth. A gyrostat consists of a massive fly-wheel concealed in a metal casing. In general, a gyrostat is a system of bodies whose relative motion does not alter the intrinsic mass distribution of the system. A solid gyrostat is an arbitrary rigid body attached to one or more axisymmetric rotors with their axes fixed in the carrier [19].

A satellite gyrostat is a solid body with statically and dynamically balanced rotors inside it. Normally, it is assumed that the angular velocity of rotation of the rotors with respect to the body of the satellite is constant and that the center of mass of the satellite moves along a circular orbit [16]. Let us consider the case of a satellite represented by a gyrostat as in [9, 10]. A satellite gyrostat is a suspended rigid body, termed *platform*, that contains one or more rigid wheels, termed *rotors*, that are spinning around fixed axes. Since the total angular momentum must stay

---

constant, a rotation of the wheels causes a global counter-rotation of the gyrost, which makes it possible to stabilize its motion (known as principle of *momentum transfer* [10]).

Spacecraft formation flying, a developing technology has the potential ability to expand the future earth observation science missions. The development of small, low-cost spacecraft formation flying spacecraft has led several implementations of the idea of collaborative sensor. A formation is defined as a set of coordinated motion of the vehicles, and it is very important of the vehicle's the relative position of each other. The three main aspects of the attitude tracking control are fixed-point, angular velocity, and the desired attitude and tracking control. For three axis stability spacecraft, control torque also need to compensate for the environmental impact, such as air resistance, and gravity gradient torques to the direction of the spacecraft drift. *These control torques can be generated from the outside, through the propeller, the internal momentum wheel, or by a combination of both.* The target tracking trajectory by tracking the command of the sun also can make the solar cell array axis remain perpendicular to the direction of the sun, and sensor tracking target. (Adapted from [23].)

Assuming that the center of the gyrost is fixed in space, one may attach an inertial reference frame  $\mathcal{F}_E$  to the center and refer the position of each point of the platform in a platform-fixed reference frame  $\mathcal{F}_P$ , as shown in the Figure 4.1.

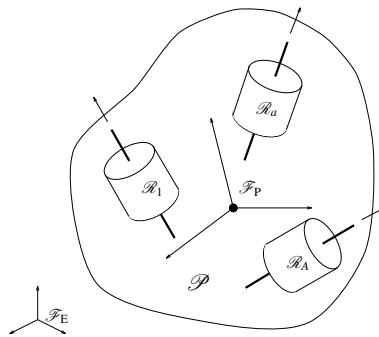


Figure 4.1: Gyrost reference frames (adapted from [10]).

The mathematical model of a gyrost satellite includes a number of constant

physical terms, which are summarized in the following matrices:

$$\left\{ \begin{array}{l} D := \text{diag} \left( \sqrt{\frac{J_y J_z}{J_x}}, \sqrt{\frac{J_x J_z}{J_y}}, \sqrt{\frac{J_x J_y}{J_z}} \right), \\ \hat{J}_g = \frac{1}{2} \begin{bmatrix} J_y - J_x + J_z & 0 & 0 \\ 0 & J_x - J_y + J_z & 0 \\ 0 & 0 & J_x + J_y - J_z \end{bmatrix}, \\ P := \frac{1}{2} \begin{bmatrix} \gamma & 0 & 0 \\ 0 & \gamma & 0 \\ 0 & 0 & -\gamma \end{bmatrix}, \end{array} \right. \quad (4.1)$$

where  $J_x > 0$ ,  $J_y > 0$  and  $J_z > 0$  denote principal moments of inertia and  $\gamma \geq 0$  is a friction coefficient.

The equations of a gyrostatt satellite may be cast in the language of Lie groups as:

$$\left\{ \begin{array}{l} C := [\kappa_1(\omega_r - \omega_x) + \kappa_2(\omega_r^3 - \omega_x^3)]\Omega_x + [\kappa_3(\omega_r - \omega_y) + \kappa_4(\omega_r^3 - \omega_y^3)]\Omega_y + \\ \quad [\kappa_5(\omega_r - \omega_z) + \kappa_6(\omega_r^3 - \omega_z^3)]\Omega_z, \\ B := J_{11}\omega_1\Omega_x + J_{22}\omega_2\Omega_y + J_{33}\omega_3(1 + b \cos(vt))\Omega_z, \\ \dot{\Omega} = D^{-1}([\hat{J}_g, \Omega^2] + [B, \Omega] - \dot{B} - \{P, \Omega\} + C)D^{-1}, \\ \dot{R} = R\Omega, \end{array} \right. \quad (4.2)$$

where  $t \in [0, 600]$  (min),  $\Omega = \omega_x\Omega_x + \omega_y\Omega_y + \omega_z\Omega_z$  and a pair of initial conditions need to be set.

The differential equation for  $\Omega$  has support in  $\mathfrak{so}(3)$ , which is a vector space isomorphic to  $\mathbb{R}^3$ . The differential equation for  $R$  has support in  $\text{SO}(3)$ , which is a curved space, hence it needs to be solved numerically by a specific method, which will be outlined in the following.

---

The numerical values of the parameters are taken from [9], namely:

$$\begin{cases} J_x = J_y = 500 \text{ kg} \cdot \text{m}^2, \\ J_z = 1000 \text{ kg} \cdot \text{m}^2, \\ J_{11}\omega_1 = J_{22}\omega_2 = 200 \text{ kg} \cdot \text{m}^2 \cdot \text{rad} \cdot \text{s}^{-1}, \\ J_{33}\omega_3 = 250 \text{ kg} \cdot \text{m}^2 \cdot \text{rad} \cdot \text{s}^{-1}, \\ \gamma = 200 \text{ kg} \cdot \text{m}^2 \cdot \text{s}^{-1}, \\ \nu = \frac{1}{20} \text{ s}^{-1}, \\ \omega_r = 0 \text{ rad} \cdot \text{s}^{-1}, \end{cases} \quad (4.3)$$

The (adimensional) amplitude  $b$  of the forcing oscillatory torque along the  $z$  axis varies in the interval  $[4.5, 6.5]$ . Moreover, the values of the controller coefficients  $\kappa_1, \dots, \kappa_6$  may be varied to emphasize or de-emphasize the role of the attitude stabilizer.

Here, we shall assume that the control torque is generated externally to the gyrostat satellite by propellers.

## 4.2 Mathematical model of quadrotor drone on $\text{SO}(3) \times \mathfrak{so}(3) \times \mathbb{R}^3$

A quadrotor is made of a body  $\mathcal{B}$  and of four rotors  $\mathcal{R}_a$ , with  $a = 1, 2, 3, 4$ , also termed *propellers*. We assume that one pair of propellers ( $a = 2$  and  $a = 4$ ) is rotating clockwise, while the other pair of propellers ( $a = 1$  and  $a = 3$ ) is rotating counterclockwise, as shown in the Figure 4.2. The rotor  $\mathcal{R}_1$  is located along the  $+x$  axis (hence the rotor  $\mathcal{R}_3$  is located along the  $-x$  axis), while the rotor  $\mathcal{R}_4$  is located along the  $+y$  axis (hence the rotor  $\mathcal{R}_2$  is located along the  $-y$  axis). The coordinates of each volume element of the drone are referred to an *earth reference frame* denoted by  $\mathcal{F}_E$ . A reference frame, denoted as  $\mathcal{F}_B$ , is attached to the body of the quadrotor, with origin in its center of mass, as shown in the Figure 4.2. By adjusting the rotors speeds, a control system may drive a quadcopter into a number of maneuvers, such as:

- **Vertical motion:** A drone can be driven into three maneuvers in the vertical plane: hovering, climbing, or descending. To hover, the net thrust of the

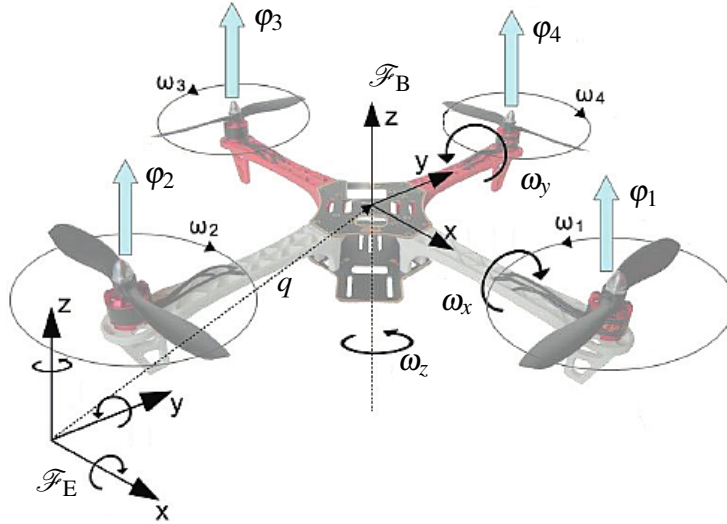


Figure 4.2: Quadcopter reference frames.

four rotors pushing the drone up must be equal to the gravitational force pulling it down. Increasing the thrust of the four rotors so that there is a non-zero upward force that is greater than the weight causes the drone to climb. Decrease the thrust causes the drone to descend vertically.

- **Turning (yawing):** Assume a drone is hovering and one wants to rotate it along its vertical axis (which is referred to as *yawing*). According to the Figure 4.2, two rotors are spinning counterclockwise and two are spinning clockwise. With the two sets of rotors rotating in opposite directions, the total angular momentum is zero. Since there is no torque on the drone, then the total angular momentum must remain constant (zero in this case). Decreasing the angular velocity of the rotors spinning clockwise and increasing the angular velocity of the rotors spinning counterclockwise, the drone rotates clockwise so that the body of the drone has an angular momentum that compensates for the total angular momentum of the rotors. Namely, the angular momentum of the rotors does not add up to zero, so the drone body must rotate. However, the total force remains equal to the gravitational force and

---

the drone continues to hover. Since the lower thrust rotors are diagonally opposite from each other, the drone can still stay balanced and does not tip.

- **Moving forwards and sideways (pitching and rolling):** In most cases, there is no difference between moving forward or backward (that is referred to as *pitching*), because the drone is symmetrical. The same holds true for side-to-side motion (which is referred to as *rolling* or *banking*). In order to fly forward, it is necessary to generate a forward component of thrust via the rotors. With reference to the Figure 4.2, increase the rotation rate of rotors 3 and 4 (the rear ones) and decrease the rate of rotors 1 and 2. The total thrust force will remain equal to the weight, so the drone will stay at the same vertical level. Also, since one of the rear rotors is spinning counterclockwise and the other clockwise, the increased rotation of those rotors will still produce zero angular momentum. The same holds true for the front rotors, and so the drone does not rotate. However, the greater force in the back of the drone means it will tilt forward. Now a slight increase in thrust for all rotors will produce a net thrust force that has a component to balance the weight along with a forward motion component.

The model includes a number of physical constants, some of which appear in the following matrices:

$$\left\{ \begin{array}{l} D := \text{diag} \left( \sqrt{\frac{J_y J_z}{J_x}}, \sqrt{\frac{J_x J_z}{J_y}}, \sqrt{\frac{J_x J_y}{J_z}} \right), \\ \hat{J}_q = \frac{1}{2} \begin{bmatrix} J_y - J_x + J_z & 0 & 0 \\ 0 & J_x - J_y + J_z & 0 \\ 0 & 0 & J_x + J_y - J_z \end{bmatrix}. \end{array} \right. \quad (4.4)$$

The model also includes four input variables, namely the spinning velocities of the four rotors  $\omega_a(t) > 0$ ,  $a = 1, 2, 3, 4$ , two state variables,  $\Omega(t) \in \mathfrak{so}(3)$  and  $v(t) \in \mathbb{R}^3$ , and two output variables,  $R(t) \in \text{SO}(3)$  and  $q(t) \in \mathbb{R}^3$ .

The equations of a quadrotor drone may be cast in a Lie-group setting as:

$$\begin{cases} T := br(\omega_4^2 - \omega_2^2)\Omega_x + br(\omega_3^2 - \omega_1^2)\Omega_y + \gamma(-\omega_1^2 + \omega_2^2 - \omega_3^2 + \omega_4^2)\Omega_z, \\ B := J_{\mathcal{R}}(-\omega_1 + \omega_2 - \omega_3 + \omega_4)\Omega_z, \\ \dot{\Omega} = D^{-1}([\hat{J}_q, \Omega^2] + [B, \Omega] - \dot{B} + T)D^{-1}, \\ \dot{R} = R\Omega, \\ \dot{v} = \frac{1}{2} \frac{b}{M_q} (\omega_1^2 + \omega_2^2 + \omega_3^2 + \omega_4^2) R e_z - p e_z - \frac{1}{M_q} \Gamma v, \\ \dot{q} = v, \end{cases} \quad (4.5)$$

for  $t \in [0, 3]$  (seconds). It is customary to make sure that, during motion, a zero residual rotor angular velocity, namely  $-\omega_1 + \omega_2 - \omega_3 + \omega_4 = 0$ , holds. In this case,  $B = 0$  and  $\dot{B} = 0$ . The parameter  $J_{\mathcal{R}}$  then disappears from the equations. The first four equations concern the orientation/attitude of the drone, while the last two equations (where  $e_z := [0 \ 0 \ 1]^T$  denotes a vertical axis) concern the translation.

This differential system contains three equations on vector spaces (the equation for  $\Omega$  has support  $\mathfrak{so}(3)$  and the equations for  $q$  and  $v$  have support  $\mathbb{R}^3$ ) and an equation on a Lie group. The numerical values of the parameters are taken from [2], namely:

$$\begin{cases} M_q = 0.650 \text{ kg}, \\ J_x = J_y = 7.5 \times 10^{-3} \text{ kg} \cdot \text{m}^2, \\ J_z = 1.3 \times 10^{-2} \text{ kg} \cdot \text{m}^2, \\ b = 3.13 \times 10^{-5}, \text{ N} \cdot \text{s}^2 \\ r = 0.23 \text{ m}, \\ \gamma = 7.5 \times 10^{-7} \text{ N} \cdot \text{m} \cdot \text{s}^2, \\ p = 9.81 \text{ m} \cdot \text{s}^{-2}, \\ \Gamma = 0.25 I_3 \text{ kg} \cdot \text{s}^{-2}. \end{cases} \quad (4.6)$$

Even though the mathematical model deals with angular velocities  $\omega_a$  as input variables, the input values are chosen to be the RPM  $n_a$  of the rotors, because this is the more natural way of setting the propeller rotation velocity. The relation between angular velocity and rotation per minute is  $\omega_a = \frac{\pi}{30} n_a$ . We recall four test experiments suggested in [3, Table 1] adapted to the present model. The rotors speed was adapted to the present case by means of a hovering design. Namely, we

---

considered the case that the thrust produced by four rotors spinning at equal speed  $\omega_h$  (the hovering speed) balances perfectly the gravitational force, formally:

$$\frac{1}{2} \frac{b}{M_q} (4\omega_h^2) = p \Rightarrow \omega_h^2 := \frac{pM_q}{2b}. \quad (4.7)$$

The resulting steady-state rotor speed in RPM (rounded to the nearest integer) reads

$$n_h := \left\lfloor \frac{30}{\pi} \sqrt{\frac{pM_q}{2b}} \right\rfloor = 3048, \quad (4.8)$$

that corresponds to a hovering velocity of about 319 rad/s.

Four typical maneuvers, and the corresponding rotors RPM (adapted from [3]), are outlined in Table 4.1. Notice that, in all four maneuvers, the residual angular

Table 4.1: Summary of four numerical experiments design, adapted from [3].

Maneuver	Rotors RPM			
	$n_1$	$n_2$	$n_3$	$n_4$
<b>Hover</b>	3048	3048	3048	3048
<b>Yaw &amp; Roll (-y)</b>	3048	3047	3048	3049
<b>Yaw &amp; Pitch (+x)</b>	3047	3048	3049	3048
<b>Pitch (+x) &amp; Roll (+y)</b>	3047	3049	3049	3047

velocity is null, namely  $\Omega_r = 0$ .

## 5. Numerical simulation of Hard-Duffing oscillator on the special orthogonal group $SO(3)$

The kinetic energy for the dynamical system in this section takes the expression  $\mathcal{K} = -\frac{1}{2}\text{tr}[V^2]$ , where  $\Omega \in \mathfrak{so}(3)$  denotes the system's angular speed matrix. The squared Riemannian distance between two sufficiently-close points  $X, Y \in SO(n)$  may be expressed in closed form as:  $d^2(X, Y) = -\text{tr}[Log^2(X^\top Y)]$ , where the symbol  $\text{tr}$  denotes matrix trace. (Note that the skew-symmetric matrix  $Log(X^\top Y)$  is semidefinite-negative, hence  $-\text{tr}[Log^2(X^\top Y)] \geq 0$ ).

According to the expressions of the geometric quantities of interest recalled above, the discrete-time version of the dynamical system (3.2) reads:

$$\begin{cases} X_{k+1} = X_k \text{Exp}(hV_k), \\ V_{k+1} = (1 - h\mu \|V_k\|^{2(\varepsilon-1)})V_k - hX_k^\top \text{grad}_{X_k} \mathcal{V}, \end{cases} \quad (5.1)$$

with  $h > 0$  being a discretization stepsize for the dynamical system and  $\varepsilon > 0$  being the exponential for nonlinear damping. The system state is represented by the pair  $(X_k, V_k) \in SO(3) \times \mathfrak{so}(3)$  for  $k \in \mathbb{N}$ . The first equation of the numerical method (5.1) represents a geodesic-based Euler-like step-forward numerical approximation of the flow associated with the first differential equation on the tangent bundle  $TSO(3)$ . The second equation represents a direct Euler-like step-forward method that takes place on a linear space, namely, the Lie algebra  $\mathfrak{so}(3)$ .

---

## 5.1 Visual rendering via a group action on a manifold

In order to achieve visual rendering of the  $\text{SO}(3)$ -trajectories generated by the non-linear oscillators, we shall be exploiting the notion of group action on a manifold.

Given a group  $\mathbb{G}$  and a smooth manifold  $\mathbb{M}$ , a *group action*  $\Lambda : \mathbb{G} \times \mathbb{M} \rightarrow \mathbb{M}$  is denoted as  $y = \Lambda_g(x)$ , where  $g \in \mathbb{G}$  and  $x, y \in \mathbb{M}$  [4]. It is worth recalling that an *orbit* of a point  $x \in \mathbb{M}$  under a group action  $\Lambda$  is defined as  $\mathbb{G}^\Lambda \cdot x := \{\Lambda_g(x) \mid g \in \mathbb{G}\}$  [4]. In the case of interest in the present report, a suitable group action is invoked in order to provide a 3-dimensional graphical rendering of trajectories generated in the Lie group of 3-dimensional rotations, which are represented by  $3 \times 3$  matrices. Therefore, we take  $\mathbb{G} = \text{SO}(3)$  and  $\mathbb{M} = \mathbb{S}^2$  and define  $\Lambda_X(p) := Xp$ , with  $X \in \text{SO}(3)$  and  $p \in \mathbb{S}^2$ . Clearly, a trajectory will be represented as a subset of  $\text{SO}(3)^\Lambda \cdot p \cong \mathbb{S}^2$ .

In other words, in the numerical simulations, the trajectories generated by the oscillators have been represented in the hyper-sphere  $\mathbb{S}^2$ . In particular, taken an arbitrary ‘seed’ on the hyper-sphere, it is multiplied by the initial rotation matrix, belonging to  $\text{SO}(3)$ . Also the reference point is obtained multiplying the starting point by the reference rotation matrix. Therefore, in this way, the starting vector assumes an initial inclination and it will oscillate around a reference inclination. Only in the non-damped case (when  $\mu = 0$ ) the reference inclination matrix is taken randomly, because in this way, better trajectories are obtained during the simulations. As the inclination matrix evolves over time, it will change its value according to the laws of the considered oscillator. So, multiplying this matrix by the initial vector belonging to  $\mathbb{S}^2$ , we will obtain, instant by instant, a vector that will belong to the sphere with a new inclination.

## 5.2 Results of numerical simulations on a hard Duffing oscillator

In this instance of a dynamical system on the Lie group  $\text{SO}(3)$ , the potential energy function takes the expression  $\mathcal{V}^{(\text{H-duf})} := -\frac{1}{2} \text{tr} [\text{Log}^2(X^\top R)] + \frac{1}{4} \kappa \text{tr} [\text{Log}^2(X^\top R)]^2$ ,

where  $X \in \text{SO}(3)$  denotes the system's orientation state matrix and  $R \in \text{SO}(3)$  denotes a reference point for the system's oscillations. Since the potential is a quartic form in the Riemannian distance (but not in the system's state), the potential might be referred to as *quartic*.

The time-discretized version of the dynamical system (3.5) on the manifold of special orthogonal matrices, associated to the hard Duffing oscillators, reads:

$$\begin{cases} X_{k+1} = X_k \text{Exp}(hV_k), \\ V_{k+1} = (1 + h\mu \text{tr}[V_k^2]^{\varepsilon-1})V_k + h(1 + \kappa d^2(X_k, R)) \text{Log}(X_k^\top R). \end{cases} \quad (5.2)$$

The Figure 5.1 illustrates the behavior of a hard Duffing oscillator on the special orthogonal group  $\text{SO}(3)$  embedded in  $\mathbb{R}^3$  in the absence of a damping term via a Lie-group action-based rendering technique.

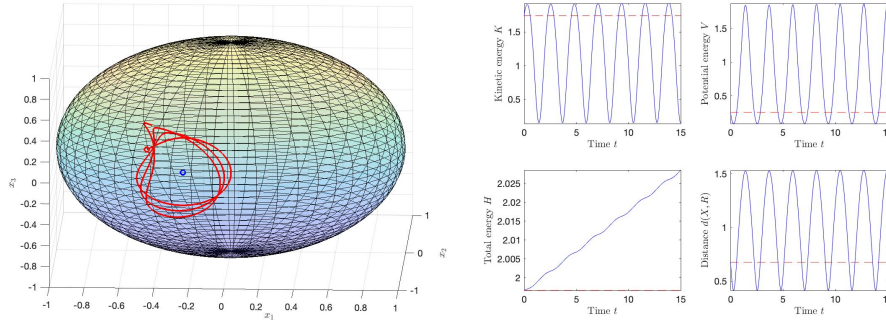


Figure 5.1: Behaviour of a hard Duffing oscillator (5.2) on the special orthogonal group  $\text{SO}(3)$ , in the absence of non-linear damping (namely,  $\mu = 0$ ). The left-hand side panel shows the trajectory on the special orthogonal group  $\text{SO}(3)$ , when the starting point and also the reference point are taken randomly, (denoted by a blue open circle) and the initial speed will be random, because related to the initial state. The parameters used in the simulation are  $\kappa = 0.5$  and  $h = 0.0005$ .

The Figure 5.2 illustrates the behavior of a hard Duffing oscillator on the special orthogonal group  $\text{SO}(3)$  embedded in  $\mathbb{R}^3$  in the presence of a damping term.

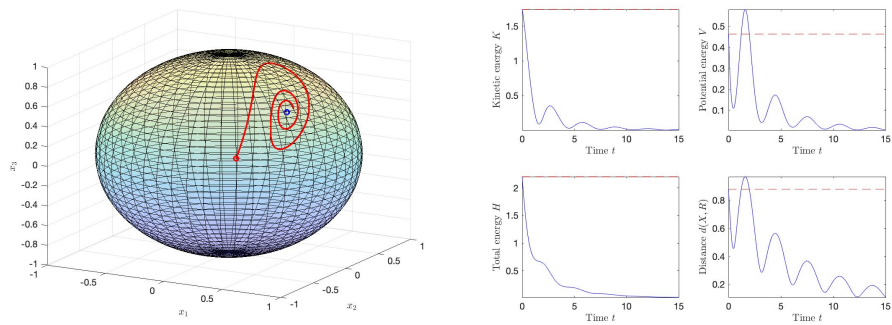


Figure 5.2: Behaviour of a hard Duffing oscillator (5.2) in the presence of non-linear damping. The left-hand panel shows the trajectory in the special orthogonal group  $SO(3)$ , when the starting point and also the reference point are taken randomly (denoted by a blue open circle) the initial speed will be random, because related to the initial state. The parameters used in the simulation are  $\kappa = 0.5$ ,  $\mu = 0.5$ ,  $\varepsilon = 1.3$  and  $h = 0.0008$ .

# 6. Numerical simulations of the gyrostat satellite and of the quadcopter drone

The present section describes the numerical methods used to implement the models of a gyrostat satellite and of a quadcopter drone. Also, this section shows the results of several numerical simulations to illustrate the behavior of the above models.

## 6.1 Numerical simulation methods

A discrete-time system to simulate numerically the dynamics of a gyrostat satellite, implemented by Euler-like stepping methods, is as follows:

$$\begin{cases} C_k := [\kappa_1(\omega_r - \omega_{x,k}) + \kappa_2(\omega_r^3 - \omega_{x,k}^3)]\Omega_x + [\kappa_3(\omega_r - \omega_{y,k}) + \kappa_4(\omega_r^3 - \omega_{y,k}^3)]\Omega_y + \\ \quad [\kappa_5(\omega_r - \omega_{z,k}) + \kappa_6(\omega_r^3 - \omega_{z,k}^3)]\Omega_z, \\ B_k := J_{11}\omega_1\Omega_x + J_{22}\omega_2\Omega_y + J_{33}\omega_3(1 + b\cos(vhk))\Omega_z, \\ \dot{B}_k := -bJ_{33}\omega_3\sin(vhk)\Omega_z, \\ \Omega_{k+1} = \Omega_k + hD^{-1}([\hat{J}_g, \Omega_k^2] + [B_k, \Omega_k] - \dot{B}_k - \{P, \Omega_k\} + C_k)D^{-1}, \\ R_{k+1} = R_k \text{Exp}(h\Omega_k), \end{cases} \quad (6.1)$$

where  $\Omega_k = \omega_{x,k}\Omega_x + \omega_{y,k}\Omega_y + \omega_{z,k}\Omega_z$ ,  $k = 0, 1, 2, \dots$  and the initial conditions are  $\Omega_0 = 0$  and  $R_0 = I_3$ . All the physical constants have the values specified in (4.3).

A discrete-time system to implement the model of the quadrotor drone, imple-

mented by a Euler-like stepping method, is:

$$\begin{cases} T_k := br(\omega_{4,k}^2 - \omega_{2,k}^2)\Omega_x + br(\omega_{3,k}^2 - \omega_{1,k}^2)\Omega_y + \gamma(-\omega_{1,k}^2 + \omega_{2,k}^2 - \omega_{3,k}^2 + \omega_{4,k}^2)\Omega_z, \\ \Omega_{r,k} := -\omega_{1,k} + \omega_{2,k} - \omega_{3,k} + \omega_{4,k}, \\ B_k := J_{\mathcal{R}}\Omega_{r,k}\Omega_z, \\ \Omega_{k+1} = \Omega_k + hD^{-1}([\hat{J}_q, \Omega_k^2] + [B_k, \Omega_k] - \frac{1}{h}(B_k - B_{k-1}) + T_k)D^{-1}, \\ R_{k+1} = R_k \text{Exp}(h\Omega_k), \end{cases} \quad (6.2)$$

to what concern the rotational component of motion, where  $k = 0, 1, 2, \dots$  and the initial conditions are  $\Omega_0 = 0$ ,  $R_0 = I_3$  and  $B_{-1} = 0$ , where all the constants take the values specified in (4.6), plus

$$\begin{cases} v_{k+1} = v_k + h\left(\frac{1}{2}\frac{b}{M_q}(\omega_{1,k}^2 + \omega_{2,k}^2 + \omega_{3,k}^2 + \omega_{4,k}^2)R_k e_z - p e_z - \frac{1}{M_q}\Gamma v_k\right), \\ q_{k+1} = q_k + h v_k, \end{cases} \quad (6.3)$$

to what concerns the translational component of motion, where  $v_0 = 0$  and  $q_0 = 0$ .

## 6.2 Results of the numerical simulation of the gyrostat satellite

In the numerical simulation of the gyrostat satellite there are two IVPs to solve on the tangent bundle of  $SO(3)$  (one related to its orientation and the other related to its angular velocity), because the satellite will change only its attitude, as opposed to the quadcopter drone which involves four IVPs.

A number of numerical simulations revealed that the inertial terms  $J_x, J_y$  and  $J_z$  can be modified, but only proportionally, so multiplying them with a real number. In this way, the state of the system will remain on  $SO(3)$  and the physical meaning of the system will be preserved, namely, we shall see the satellite rotating without any deformation. Upon setting  $J_x, J_y$  and  $J_z$  to higher values, the gyrostat satellite rotates slower, because of a major resistance of inertia, while for lower values it will move faster. In this simulation, the point that the gyrostat satellite turns around from coincides to its contact point with the  $x - y$  plane.

A real-world gyrostat should remain motionless on its axis. But since we shall

use this system to test synchronization, it would be useless for it to remain stationary, and therefore it is made to oscillate in the simulation.

The Figure 6.1 shows the orientation of the gyrostat, during the oscillation, in four different moments. It can be seen that the point of contact with the  $x - y$  plane does not change, since the oscillation occurs around this point. In this numerical simulation, the value  $h = 10^{-3}$  has been set.

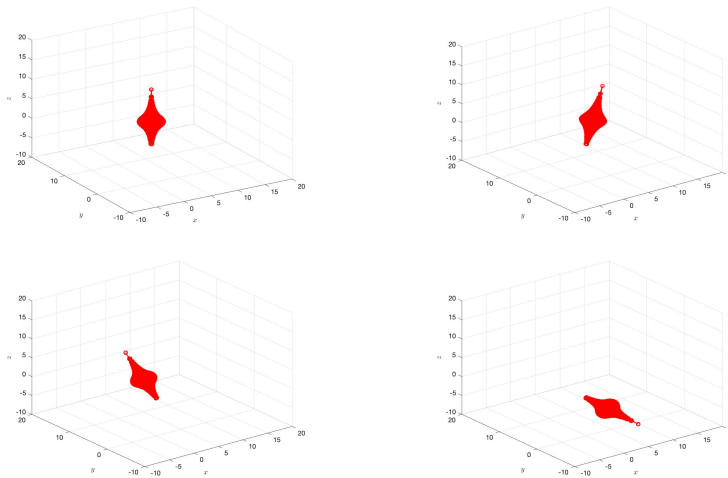


Figure 6.1: Behaviour of a gyrostat oscillating around its contact point with the  $x - y$  plane, that is the origin. In the top-left panel it can be seen the gyrostat at  $k = 1,000$ , in the top-right panel at  $k = 20,000$ , in the bottom-left panel with  $k = 30,000$  and in the bottom-right panel with  $k = 45,000$ .

### **6.3 Results of the numerical simulation of the quadcopter drone**

The quadcopter drone exhibits a more complex dynamics, characterized by two pairs of IVPs, one for translational component of motion on the 3-dimensional real space (affecting the position of its center of mass) and one for the rotational component of motion on the  $SO(3)$  manifold (affecting its attitude). In the whole lot of the following numerical simulations, the value  $h = 10^{-3}$  has been chosen.

---

The first simulation concerns only the rotational component of motion, whose computation involves only one of the two pairs of differential equations. In fact, it can be seen from the model (4.5) of the drone that the rotational movement is completely independent of the translational one.

In the the Figure 6.2 it is possible to observe that the drone oscillates around the center of mass, which however stay still in space. Instead it can not independently achieve any translation, since, as it appears from the mathematical model, the translational component of motion is related to the orientation of a drone.

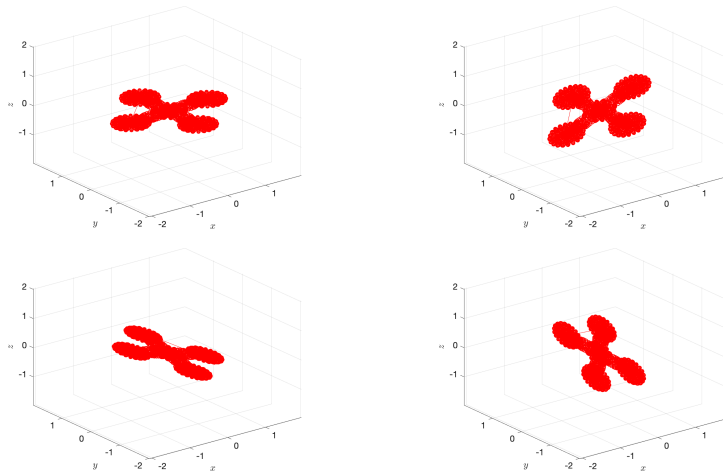


Figure 6.2: Behaviour of the quadrotor drone (6.2) that performs only rotational movements, in which it oscillates around the center of mass, that is in the origin of the reference system.

Complete simulations were obtained to show a drone which moves along a trajectory in  $\mathbb{R}^3$ , changing its attitude according a chosen maneuver. In particular the simulations concern four different maneuvers:

- **Hover**, that describes the static behavior of the drone on the space remaining on its position parallel to  $x$ - $y$  plane. In this situation, the rotors of the drone have only to overcome gravity (in absence of other external forces which are not described by our model). The obtained results are shown in the Figure 6.3.

- **Yaw and roll**, with the drone turning and moving along the negative  $y$  direction. The obtained results are shown in the Figure 6.4.
- **Yaw and pitch**, with the drone turning and moving along the positive  $x$  direction. The obtained results are shown in the Figure 6.5.
- **Pitch and roll**, with the drone turning and moving along the positive direction of both  $x$  and  $y$ . The obtained results are shown in the Figure 6.6.

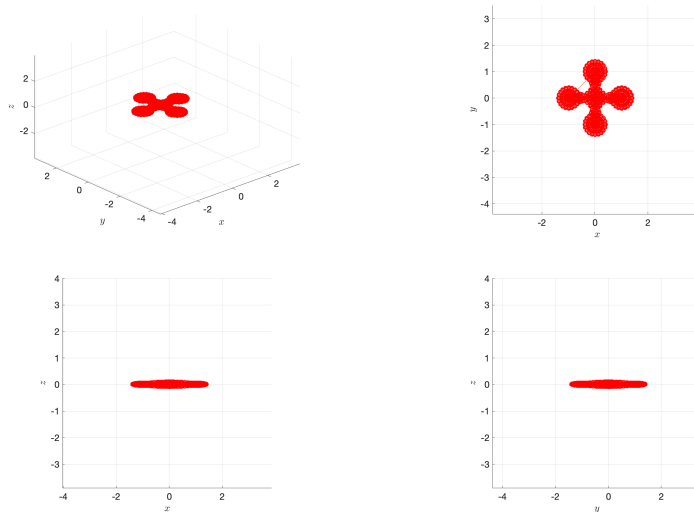


Figure 6.3: Behaviour of a drone performing a hover maneuver. It is possible to see that the object remains parallel to the  $x$ - $y$  plane thus maintaining the same height. In the top-left panel it can be seen a 3D view, while in the top-right panel there is a  $x$ - $y$  view, in the bottom-left panel there is a  $x$ - $z$  view and in the bottom-right panel there is a  $y$ - $z$  view.

These maneuvers are implemented by changing the speed of the four rotors of the drone. When their speed is the same the drone will move vertically upwards or downwards or it will remain on its position.

There exists a particular value of rotors speed, as given in (4.8), that approximately balances the gravitational acceleration, so that the resulting force acting on the system is null and the drone does not move. For larger values of rotors speed,

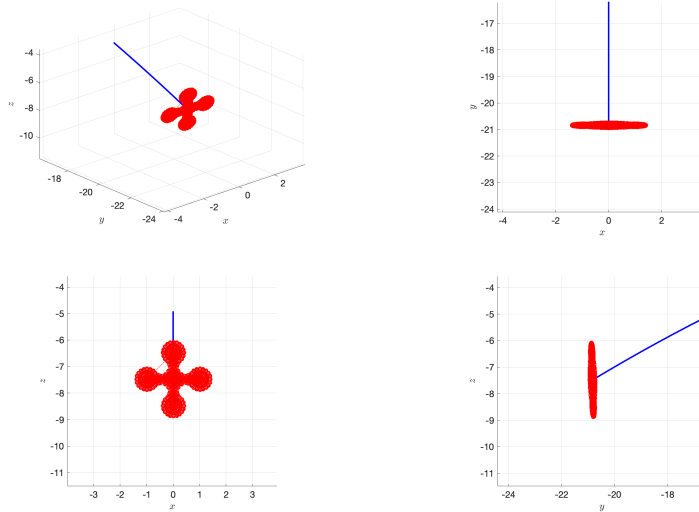


Figure 6.4: Behaviour of a drone performing a yaw and roll maneuver. It is possible to see that the object is turning and moving along the negative y direction.

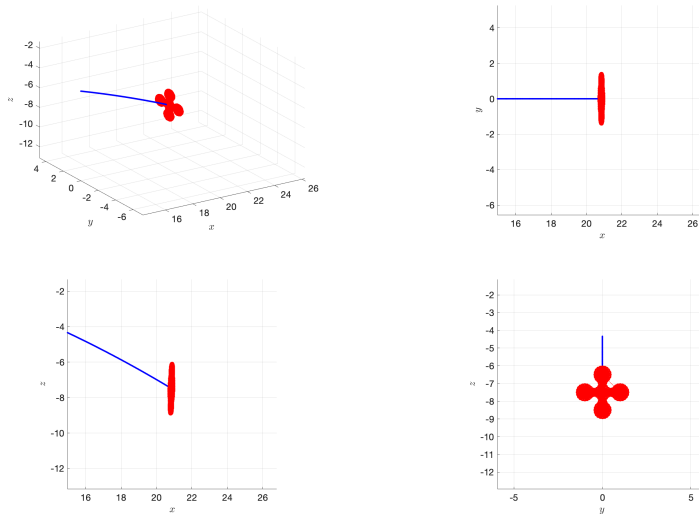


Figure 6.5: Behaviour of a drone performing a yaw and pitch maneuver. It is possible to see that the object is turning and moving along the positive x direction.

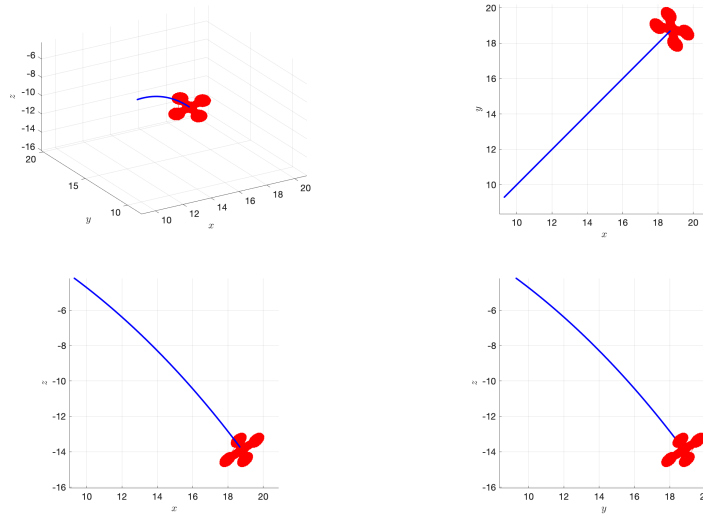


Figure 6.6: Behaviour of a drone performing a pitch and roll maneuver. It is possible to see that the object is turning and moving along the positive direction of both  $x$  and  $y$  axes.

the drone will be subjected to a vertical lift and for smaller values it will move downwards vertically.

As already mentioned, the differential equation involving the translational component of motion depends from rotational parameters, while the rotational component of motion is not influenced by the translational one. For this reason it has firstly been possible to simulate only the rotational dynamics of the drone, because it can be considered separately being independent from translation.

# 7. Non-linear control of dynamical systems on Lie groups

The present section recalls a classical regulation theory, namely the proportional-integral-derivative (PID) control theory, for second-order dynamical systems whose state-space is  $\mathbb{R}^n$ , and presents an extension of such theory to Lie groups (L-PID). In addition, the present section illustrates an application of the proposed L-PID control theory to the time-synchronization of the motions of two dynamical systems, and in particular it is first applied to two Hard-Duffing oscillators, thus constructing a 'Toy Problem', and then to two real systems, as gyrostat satellites and drones.

## 7.1 Proportional-integral-derivative control theory

The proportional-integral-derivative control (PID) scheme is perhaps the most popular regulation theory [1]. The general idea to control a dynamical system into approaching a desired state trajectory is to compute an error signal and a control signal as a linear combination of the error signal itself (proportional control), of the time-derivative of the error signal (derivative control) and of an accumulated error signal (integral control).

Increasing the proportional term coefficient  $\kappa_p$  makes the follower system be more "ready", which means using more energy, because the control effort would be larger and it could also be useless to increase this term too much because it could cause a long series of overshoots with a consequent transient. The derivative

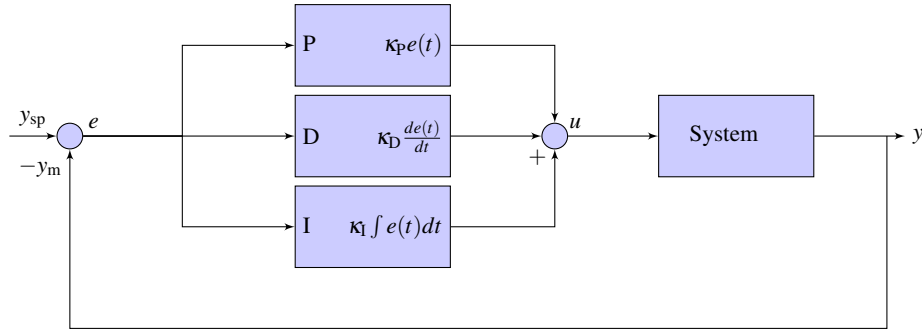


Figure 7.1: Classical PID control scheme, where  $y_{sp}$  denotes the set point,  $y_m$  denotes a measure of the controlled variable  $y$ ,  $u$  denotes a control signal and  $e$  denotes an error signal, which quantifies the discrepancy between the measured controlled variable and the set point.

term has the effect to stabilize the dynamics of the controlled system. The larger the coefficient  $\kappa_D$ , the lesser the oscillations around the set point. Finally, the integrative term is important to give to the controlled system some interesting and fundamental properties like error that tends to zero with respect to the set point and to reduce the impact of disturbances on the close loop system. Unfortunately, another effect of this term is to contrast the stabilization property of the derivative term, making the controlled system less stable and the convergence to the set point slower. The weight of its action is given by  $\kappa_I$ .

All these known properties of PID can be extended on the case of control of systems whose state is located in Lie groups.

Note that, for a second-order system, it is often impossible to control the state-velocity directly as it is only possible to control the state-acceleration (as in a mass-spring-damper system, where the spring and the damper produce mechanical forces that affect the acceleration of the mass).

## 7.2 Extension of PID regulation to Lie groups (L-PID)

The purpose of feedback control is to drive the state  $X(t)$  of a Lie-group dynamical system (2.2) towards a reference point, which may be moving over time, denoted

---

by  $Z(t) \in \mathbb{G}$ . The first step consists in defining an *error field* that generalizes the Euclidean error  $e(t) = z(t) - x(t)$  for the standard case that  $\mathbb{G} = \mathbb{R}^n$ .

We propose that a second-order, L-PID controlled dynamical system be designed as:

$$\begin{cases} \frac{d}{dt}(X^{-1}(t) \cdot \dot{X}(t)) = X^{-1}(t) \cdot \mathbb{S}(t, X(t), V(t)) + U(t), \in \mathfrak{g} \text{ (Second-order dynamical system)} \\ E(t) := X^{-1}(t) \cdot \log_{X(t)} Z(t) \in \mathfrak{g}, \text{ (Control error)} \\ \Psi(t) := \int_0^t E(\tau) d\tau \in \mathfrak{g}, \text{ (Integrated control error)} \\ \mathcal{E}(t) := Z^{-1}(t) \cdot \dot{Z}(t) - X^{-1}(t) \cdot \dot{X}(t) \in \mathfrak{g}, \text{ (Control error velocity)} \\ U(t) := \kappa_P E(t) + \kappa_I \Psi(t) + \kappa_D \mathcal{E}(t) + U_C(t) \in \mathfrak{g}, \text{ (Control field)}. \end{cases} \quad (7.1)$$

with  $U_C(t)$  to be defined.

Taking the derivative of the error velocity field  $\mathcal{E}(t)$  leads to:

$$\dot{\mathcal{E}} = \frac{d}{dt}(Z^{-1} \cdot \dot{Z}) - X^{-1} \cdot \mathbb{S}(t, X, V) - U. \quad (7.2)$$

Plugging the definition of the control field given in (7.1) into the equation (7.2) yields

$$\dot{\mathcal{E}} = \frac{d}{dt}(Z^{-1} \cdot \dot{Z}) - X^{-1} \cdot \mathbb{S}(t, X, V) - \kappa_P E - \kappa_I \Psi - \kappa_D \mathcal{E} - U_C. \quad (7.3)$$

The purpose of the term  $U_C$  is to cancel those terms in the tight-hand side of the above expression that do not depend on the error-type fields  $(E, \mathcal{E}, \Psi)$  [15], namely, we set:

$$U_C := \frac{d}{dt}(Z^{-1} \cdot \dot{Z}) - X^{-1} \cdot \mathbb{S}(t, X, V). \quad (7.4)$$

The resulting error dynamics (7.2) is governed by the equation:

$$\dot{\mathcal{E}} + \kappa_P E + \kappa_I \Psi + \kappa_D \mathcal{E} = 0. \quad (7.5)$$

The above second-order error system is characterized by the following important result.

**Theorem 7.2.1.** *The error system (7.5) converges asymptotically to the state zero as long as the compatibility condition  $X^{-1} \cdot \log_X Z = -Z^{-1} \cdot \log_Z X$  holds true,  $\kappa_P >$*

0,  $\kappa_D \geq 0$ ,  $\kappa_I = \tilde{\kappa}_I \langle \Omega, \mathcal{E} \rangle_{\mathfrak{g}}$ , with  $\tilde{\kappa}_I \geq 0$  (at least one among  $\kappa_D$  and  $\tilde{\kappa}_I$  must differ from zero).

*Proof.* The convergence of the synchronization error to zero is proven by showing that the following function is Lyapunov:

$$\mathcal{W}(X, Z) := \frac{1}{2} \langle \mathcal{E}, \mathcal{E} \rangle_{\mathfrak{g}} + \frac{\kappa_P}{2} d^2(X, Z). \quad (7.6)$$

Since  $\kappa_P > 0$ , it holds that  $\mathcal{W}(X, Z) \geq 0$ .

Let us consider the first term  $\langle \mathcal{E}, \mathcal{E} \rangle_{\mathfrak{g}}$ , whose time-derivative reads:

$$\frac{d}{dt} \langle \mathcal{E}, \mathcal{E} \rangle_{\mathfrak{g}} = \langle \dot{\mathcal{E}}, \mathcal{E} \rangle_{\mathfrak{g}} + \langle \mathcal{E}, \dot{\mathcal{E}} \rangle_{\mathfrak{g}} = 2 \langle \dot{\mathcal{E}}, \mathcal{E} \rangle_{\mathfrak{g}}. \quad (7.7)$$

Let us now consider the second term  $d^2(X, Z)$ . According to the equation (2.1) and the definition of control error field given in (7.1), it turns out that

$$\begin{cases} \text{grad}_X d^2(X, Z) = -2 \log_X Z = -2X \cdot E, \\ \text{grad}_Z d^2(X, Z) = -2 \log_Z X = 2Z \cdot E \text{ (by the compatibility condition),} \\ \frac{d}{dt} d^2(X, Z) = \langle \text{grad}_X d^2(X, Z), \dot{X} \rangle_X + \langle \text{grad}_Z d^2(X, Z), \dot{Z} \rangle_Z. \end{cases} \quad (7.8)$$

Therefore, it can be seen that the derivative  $\frac{d}{dt} d^2(X, Z)$  takes the expression:

$$\begin{aligned} \frac{d}{dt} d^2(X, Z) &= \langle -2X \cdot E, \dot{X} \rangle_X + \langle 2Z \cdot E, \dot{Z} \rangle_Z \\ &= -2 \langle X^{-1} \cdot X \cdot E, X^{-1} \cdot \dot{X} \rangle_{\mathfrak{g}} + 2 \langle Z^{-1} \cdot Z \cdot E, Z^{-1} \cdot \dot{Z} \rangle_{\mathfrak{g}} \\ &= 2 \langle E, Z^{-1} \cdot \dot{Z} - X^{-1} \cdot \dot{X} \rangle_{\mathfrak{g}} \\ &= 2 \langle E, \mathcal{E} \rangle_{\mathfrak{g}}. \end{aligned} \quad (7.9)$$

In conclusion, deriving the function  $\mathcal{W}$  with respect to the time gives:

$$\begin{aligned} \dot{\mathcal{W}} &= \kappa_P \langle E, \mathcal{E} \rangle + \langle \dot{\mathcal{E}}, \mathcal{E} \rangle_{\mathfrak{g}} \\ &= \langle -\kappa_P E - \kappa_I \Psi - \kappa_D \mathcal{E}, \mathcal{E} \rangle_{\mathfrak{g}} + \kappa_P \langle E, \mathcal{E} \rangle_{\mathfrak{g}} \\ &= -\kappa_D \langle \mathcal{E}, \mathcal{E} \rangle_{\mathfrak{g}} - \tilde{\kappa}_I \langle \Psi, \mathcal{E} \rangle_{\mathfrak{g}}^2, \\ &\leq 0, \end{aligned} \quad (7.10)$$

since the coefficients are non-negative and at least one of them is non-zero, which proves the assertion.  $\square$

---

The Theorem 7.2.1 is based on the assumption that  $X^{-1} \cdot \log_X Z = -Z^{-1} \cdot \log_Z X$ . It is important to remark that the property  $\log_Z X = -Z \cdot X^{-1} \cdot \log_X Z$  is a special feature of a Lie group and of its logarithmic map and it does not extend to other tangent fields (namely, if  $P^{X \rightarrow Z}$  denotes parallel transport, in general  $P^{X \rightarrow Z} \neq Z \cdot X^{-1} \cdot$ .)!

Let us consider two examples where this property can be easily verified:

- **Special orthogonal group:** In this group, inversion coincides to matrix transposition and  $\log_X Z := X \text{Log}(X^\top Z)$ , therefore, it can be readily verified that  $X^\top \log_X Z = -Z^\top \log_Z X$  is implied by  $\text{Log}(X^\top Z) = -\text{Log}(Z^\top X)$ . However, parallel transport in  $\text{SO}(3)$  reads  $P^{X \rightarrow Z}(V) := X \sqrt{X^\top Y} X^\top V \sqrt{X^\top Y}$ , which is apparently very different from  $ZX^\top V$  (which is, in fact, a possible instance of *vector transport*).
- **Group of symmetric, positive-definite matrices:** In this group, each tangent space coincides directly to the Lie algebra, therefore left translation is an identity. Moreover,  $\log_X Z := \text{Log}(Z) - \text{Log}(X)$ , which verifies the property.

Notice that positional control implies velocity control (although the converse is not true, in general).

### 7.2.1 Extension of PID regulation to the 3D rotation group

In this subsection, we refer explicitly to the Lie group of 3D rotations, that is denoted as  $\text{SO}(3)$ . A second-order dynamical system evolving on  $\text{SO}(3)$  is described by the following two coupled equations

$$\begin{cases} \dot{V} = X^\top \mathbb{S}(t, X, V), & \text{(Velocity-transition equation)} \\ \dot{X} = X V. & \text{(Position-transition equation)} \end{cases} \quad (7.11)$$

The first step to design a feedback control system consists in defining an *error field* that generalizes the Euclidean error  $e(t) = z(t) - x(t)$  for the standard case that  $\mathbb{G} = \mathbb{R}^n$ .

We propose that a second-order, controlled dynamical system on  $\text{SO}(3)$  be designed as:

$$\left\{ \begin{array}{l} \dot{V}(t) = X^\top(t)\mathbb{S}(t, X(t), V(t)) + U(t) \in \mathfrak{so}(3), \text{ (Second-order dynamical system)} \\ E(t) := \text{Log}(X^\top(t)Z(t)) \in \mathfrak{so}(3), \text{ (Control error)} \\ \Psi(t) := \int_0^t E(\tau)d\tau \in \mathfrak{so}(3), \text{ (Integrated control error)} \\ \mathcal{E}(t) := Z^\top(t)\dot{Z}(t) - V(t) \in \mathfrak{so}(3), \text{ (Control error velocity)} \\ U_C(t) := \frac{d}{dt}(Z^\top(t)\dot{Z}(t)) - X^\top(t)\mathbb{S}(t, X(t), V(t)) \in \mathfrak{so}(3), \text{ (Cancelling component of the control field)} \\ U(t) := \kappa_P E(t) + \kappa_I \Psi(t) + \kappa_D \mathcal{E}(t) + U_C(t) \in \mathfrak{so}(3). \text{ (Control field)} \end{array} \right. \quad (7.12)$$

The above control method arose as a special case of a general error feedback control theory on Lie groups (L-PID) explained in the section (7.2). The resulting error dynamics is governed by the equation:

$$\dot{\mathcal{E}} + \kappa_P E + \kappa_I \Psi + \kappa_D \mathcal{E} = 0. \quad (7.13)$$

The above second-order error system is characterized by the following important result.

**Theorem 7.2.2** (Adapted from 7.2.1). *The error system (7.13) converges asymptotically to the state zero as long as  $\kappa_P > 0$ ,  $\kappa_D \geq 0$ ,  $\kappa_I = \tilde{\kappa}_I \langle \Psi, \mathcal{E} \rangle_{\mathfrak{so}(3)}$ , with  $\tilde{\kappa}_I \geq 0$  (at least one among  $\kappa_D$  and  $\tilde{\kappa}_I$  must differ from zero).*

### 7.3 Control efforts

The notion of *control effort* refers to a quantification of the magnitude of a control field, which is related to the energy consumption of the actuators and is used to evaluate the suitability of the actuators with respect to a given control goal [13]. Formally, we define a global control effort function  $\sigma : T\mathbb{M} \rightarrow \mathbb{R}$  as:

$$\sigma := \frac{1}{2} \|U\|_{\mathfrak{g}}^2. \quad (7.14)$$

Likewise, we define a control effort function  $\sigma_C : T\mathbb{M} \rightarrow \mathbb{R}$  and a function  $\sigma_{\text{PID}} : T\mathbb{M} \rightarrow \mathbb{R}$  associated to the ‘cancelling’ component of the control field and to the

---

PID component of the same control field, as:

$$\sigma_C := \frac{1}{2} \|U_C\|_{\mathfrak{g}}^2, \quad \sigma_{\text{PID}} := \frac{1}{2} \|U - U_C\|_{\mathfrak{g}}^2. \quad (7.15)$$

It is important to evaluate the control efforts associated to the different components of the above-proposed L-PID control schemes. It is clear that the control effort  $\sigma_{\text{PID}}$  is directly related to the parameters  $\kappa_P$ ,  $\kappa_I$ ,  $\kappa_D$ .

## 7.4 Application of L-PID to time-synchronization of second-order systems

Synchronization of systems on Lie groups is an instance of non-linear control where the reference trajectory is generated by a dynamical system (which may coincide with, or differ from, the controlled system). The dynamical system that provides a reference is termed *leader*, described by a state-transition operator  $\mathbb{S}_L$ , while the controlled system will be referred to as *follower*, described by a state-transition operator  $\mathbb{S}_F$ . We suggest the following leader-follower synchronization scheme:

$$\left\{ \begin{array}{l} \dot{Z}(t) = Z(t)W(t), \quad \dot{W}(t) = Z^\top \mathbb{S}_L(t, Z(t), W(t)), \quad t \geq 0, \quad (\text{Leader dynamical system}) \\ \dot{X}(t) = X(t)V(t), \quad \dot{V}(t) = X^\top \mathbb{S}_F(t, X(t), V(t)) + U(t), \quad (\text{Follower dynamical system}) \\ E(t) := \text{Log}(X^\top(t)Z(t)), \quad (\text{Control error}) \\ \Psi(t) := \int_0^t E(\tau) d\tau, \quad (\text{Integrated control error}) \\ \mathcal{E}(t) := W(t) - V(t), \quad (\text{Control error velocity}) \\ U_C := \dot{W}(t) - X^\top(t) \mathbb{S}(t, X(t), V(t)), \quad (\text{Cancelling component of the control field}) \\ U(t) := \kappa_P E(t) + \kappa_I \Psi(t) + \kappa_D \mathcal{E}(t) + U_C(t), \quad (\text{Control field}). \end{array} \right. \quad (7.16)$$

In the case of synchronization, the term  $U_C$  apparently ‘cancels’ the internal dynamics of the follower system and replaces it with a copy of the internal dynamics of the leader system.

In order to implement the leader system, the controlled follower system and the control scheme on a computing platform, it is necessary to come up with discrete-time versions of the equations (7.16).

The first step consists in replacing the continuous-time variable  $t$  with a discrete-time index  $k = 0, 1, 2, \dots$  related by  $t = hk$ , where  $h > 0$  is a discretization stepsize that is generally much smaller than 1. Likewise, the continuous-time variables describing the dynamics of the systems as well as the control field are replaced by their discrete-time counterparts:

$$\left\{ \begin{array}{l} Z_{k+1} := Z_k \text{Exp}(h W_k), \quad k = 0, 1, 2, \dots, \\ W_{k+1} := W_k + h Z^\top \mathbb{S}_L(hk, Z_k, W_k), \\ X_{k+1} := X_k \text{Exp}(h V_k), \\ V_{k+1} := V_k + h X^\top \mathbb{S}_F(hk, X_k, V_k) + h U_k, \\ E_k := \text{Log}(X_k^\top Z_k), \\ \mathcal{E}_k := W_k - V_k, \\ \Psi_k := h \sum_{i=0}^k E_i, \quad (\text{Numerically-accumulated control error}) \\ U_{C,k} := \begin{cases} -\mathbb{S}_F(0, X_0, V_0), & \text{if } k = 0, \\ \frac{1}{h}(W_k - W_{k-1}) - \mathbb{S}_F(hk, X_k, V_k), & \text{if } k > 0, \end{cases} \\ U_k := \kappa_P E_k + \kappa_I \Psi_k + \kappa_D \mathcal{E}_k + U_{C,k}, \end{array} \right. \quad (7.17)$$

where  $X_0, Z_0 \in \text{SO}(3)$ ,  $V_0, W_0 \in \mathfrak{so}(3)$  are given initial states. The dynamics of the leader system is described by the variables pair  $(Z_k, W_k) \in \text{SO}(3) \times \mathfrak{so}(3)$  and the dynamics of the follower is described by the variables pair  $(X_k, V_k) \in \text{SO}(3) \times \mathfrak{so}(3)$ . The flow of the continuous-time dynamics of the systems has been approximated numerically by a forward Euler stepping [7], while special care has been devoted to the numerical approximation of the cumulative error control term  $\Psi_k$ .

In the next section 8, the internal dynamics of the two systems are described by two hard Duffing oscillators formulated on the Lie group  $\text{SO}(3)$ . In particular, these oscillators are described by:

$$\left\{ \begin{array}{l} \mathbb{S}_L(t, Z, W) = -\mu \|ZW\|_Z^{2(\varepsilon-1)} ZW + [1 + \kappa d^2(Z, R_L)] \log_Z(R_L), \\ \mathbb{S}_F(t, X, V) = -\mu \|XV\|_X^{2(\varepsilon-1)} XV + [1 + \kappa d^2(X, R_F)] \log_X(R_F), \end{array} \right. \quad (7.18)$$

where  $\mu = 0$ , since the friction-type damping (dissipative force) must be null to make the body oscillate continuously, while  $R_L \in \text{SO}(3)$  and  $R_F \in \text{SO}(3)$  denote the reference attitudes of the leader and follower.

---

The leader oscillator may be implemented by the equations:

$$\begin{cases} Z_{k+1} = Z_k \text{Exp}(hW_k), \\ W_{k+1} = W_k + h(1 + \kappa d^2(Z_k, R_L)) \text{Log}(Z_k^\top R_L). \end{cases} \quad (7.19)$$

The controlled follower oscillator may be implemented by the equations:

$$\begin{cases} X_{k+1} = X_k \text{Exp}(hV_k), \\ V_{k+1} = V_k + h(1 + \kappa d^2(X_k, R_F)) \text{Log}(X_k^\top R_F) + hU_k, \end{cases} \quad (7.20)$$

where  $U_k$  denotes the control signal generated by the L-PID controller (cf. (7.17)).

## 7.5 Application of L-PID to time-synchronization of two oscillators

The aim of the study is to succeed in synchronizing two gyrostats, with different internal dynamics (in particular the moments of inertia along the three axes have been changed). Synchronization is sought among two gyrostats, a leader and a follower. The first one oscillates independently to the second one, according to its internal dynamics and parameters. To the follower, instead, is not applied the control signal  $C$ , used to rotate the gyrostat at a reference speed  $\omega_r$ , but the Lie-algebra field generated by the PID controller.

As explained in the Subsection 4.1, the gyrostat performs oscillations around its point of contact with the  $x - y$  plane, therefore it only performs rotations and not translations. It is important to keep in mind that the gyrostat, being a second-order system, can only be controlled through a mechanical torque, which is exactly generated by the controller.

The leader gyrostat is described by the continuous time system:

$$\begin{cases} C := [\kappa_1(\omega_r - \omega_x) + \kappa_2(\omega_r^3 - \omega_x^3)]\Omega_x + [\kappa_3(\omega_r - \omega_y) + \kappa_4(\omega_r^3 - \omega_y^3)]\Omega_y + \\ \quad [\kappa_5(\omega_r - \omega_z) + \kappa_6(\omega_r^3 - \omega_z^3)]\Omega_z, \\ D_L := \text{diag} \left( \sqrt{\frac{J_{L,y}J_{L,z}}{J_{L,x}}}, \sqrt{\frac{J_{L,x}J_{L,z}}{J_{L,y}}}, \sqrt{\frac{J_{L,x}J_{L,y}}{J_{L,z}}} \right), \\ \hat{J}_{L,g} = \frac{1}{2} \begin{bmatrix} J_{L,y} - J_{L,x} + J_{L,z} & 0 & 0 \\ 0 & J_{L,x} - J_{L,y} + J_{L,z} & 0 \\ 0 & 0 & J_{L,x} + J_{L,y} - J_{L,z} \end{bmatrix}, \\ \dot{W} = D_L^{-1} ([\hat{J}_{L,g}, W^2] + [B, W] - \dot{B} - \{P, W\} + C) D_L^{-1}, \\ \dot{Z} = ZW, \end{cases} \quad (7.21)$$

where  $W = \omega_x\Omega_x + \omega_y\Omega_y + \omega_z\Omega_z$  and all the constants used have the values specified in (4.3). The follower gyrostat is described by the continuous time system:

$$\begin{cases} D_F := \text{diag} \left( \sqrt{\frac{J_{F,y}J_{F,z}}{J_{F,x}}}, \sqrt{\frac{J_{F,x}J_{F,z}}{J_{F,y}}}, \sqrt{\frac{J_{F,x}J_{F,y}}{J_{F,z}}} \right), \\ \hat{J}_{F,g} = \frac{1}{2} \begin{bmatrix} J_{F,y} - J_{F,x} + J_{F,z} & 0 & 0 \\ 0 & J_{F,x} - J_{F,y} + J_{F,z} & 0 \\ 0 & 0 & J_{F,x} + J_{F,y} - J_{F,z} \end{bmatrix}, \\ \dot{V} = D_F^{-1} ([\hat{J}_{F,g}, V^2] + [B, V] - \dot{B} - \{P, V\}) D_F^{-1} + U, \\ \dot{X} = XV, \end{cases} \quad (7.22)$$

where all the constants used have the values specified in (4.3), except for the values of the inertia tensor  $J_{F,y}, J_{F,x}, J_{F,z}$  which were multiplied by 3. The leader system is described by the variables  $(Z, W) \in \text{SO}(3) \times \mathfrak{so}(3)$  and the follower system by  $(X, V) \in \text{SO}(3) \times \mathfrak{so}(3)$ . The control signal generated by the PID controller is denoted as  $U$ , and it is defined, according to the general theory developed in the Subsection 7.2, through the following equations:

$$\begin{cases} E(t) := \text{Log}(X^\top(t)Z(t)), \quad \mathcal{E}(t) := W(t) - V(t), \quad \Psi(t) := \int_0^t E(\tau) d\tau, \\ \mathbb{S}_F(t, X, V) := D_F^{-1} ([\hat{J}_{F,g}, V^2] + [B, V] - \dot{B} - \{P, V\}) D_F^{-1}, \\ U_C(t) := \dot{W}(t) - \mathbb{S}_F(t, X, V), \\ U(t) := \kappa_P E(t) + \kappa_I \Psi(t) + \kappa_D \mathcal{E}(t) + U_C(t) \end{cases} \quad (7.23)$$

A discrete time systems implementing the leader gyrostat and follower gyrostat, realized by a forward Euler method and used in the simulations, are laid out in the following. The equations for the leader gyrostat read:

$$\begin{cases} C_k := [\kappa_1(\omega_r - \omega_{x,k}) + \kappa_2(\omega_r^3 - \omega_{x,k}^3)]\Omega_x + [\kappa_3(\omega_r - \omega_{y,k}) + \kappa_4(\omega_r^3 - \omega_{y,k}^3)]\Omega_y + \\ \quad [\kappa_5(\omega_r - \omega_{z,k}) + \kappa_6(\omega_r^3 - \omega_{z,k}^3)]\Omega_z, \\ B_k := J_{11}\omega_1\Omega_x + J_{22}\omega_2\Omega_y + J_{33}\omega_3(1 + b\cos(vhk))\Omega_z, \\ \dot{B}_k := -J_{33}vb\omega_3\sin(vhk)\Omega_z, \\ W_{k+1} = W_k + hD_L^{-1}([\hat{J}_{L,g}, W_k^2] + [B_k, W_k] - \dot{B}_k - \{P, W_k\} + C_k)D_L^{-1}, \\ Z_{k+1} = Z_k\text{Exp}(hW_k), \end{cases} \quad (7.24)$$

where  $W_k = \omega_{x,k}\Omega_x + \omega_{y,k}\Omega_y + \omega_{z,k}\Omega_z$ . The equations for the follower gyrostat read:

$$\begin{cases} B_k := J_{11}\omega_1\Omega_x + J_{22}\omega_2\Omega_y + J_{33}\omega_3(1 + b\cos(vhk))\Omega_z, \\ \dot{B}_k := -J_{33}vb\omega_3\sin(vhk)\Omega_z, \\ V_{k+1} = V_k + hD_F^{-1}([\hat{J}_{F,g}, V_k^2] + [B_k, V_k] - \dot{B}_k - \{P, V_k\})D_F^{-1} + hU_k, \\ X_{k+1} = X_k\text{Exp}(hV_k). \end{cases} \quad (7.25)$$

In the discrete-time version, the leader system is described by the variables  $(Z_k, W_k) \in \text{SO}(3) \times \mathfrak{so}(3)$  and the follower system by  $(X_k, V_k) \in \text{SO}(3) \times \mathfrak{so}(3)$ , while the discrete time version of the control signal generated by the PID controller is denoted as  $U_k$ , and it is computed by the following equation:

$$\begin{cases} E_k := \text{Log}(X_k^{-1}Z_k), \\ \mathcal{E}_k := W_k - V_k, \\ \Psi_k := h\sum_{i=0}^k E_i, \text{ (Numerically-accumulated control error)} \\ U_{C,k} := \begin{cases} -\mathbb{S}_F(0, X_0, V_0), & \text{if } k = 0, \\ \frac{1}{h}(W_k - W_{k-1}) - \mathbb{S}_F(hk, X_k, V_k), & \text{if } k > 0, \end{cases} \\ U_k := \kappa_P E_k + \kappa_I \Psi_k + \kappa_D \mathcal{E}_k + U_{C,k}, \end{cases} \quad (7.26)$$

## 7.6 Application of L-PID to the time-synchronization of the attitude of two quadrotor drones

Even in this case, synchronize two real objects, two quadrotor drones, is sought. We shall assume that the two drones were described by the same mathematical

model and with the same constants. The main difference between the follower and the leader is how their dynamics is determined. In fact, the dynamics of the leader is governed by the mechanical torque  $T$  generated by the propellers, that are assumed to be constant, as described in the system (6.3). The control field for the follower, like in the gyrostat case, is produced by the L-PID controller.

Unlike the gyrostat, the drone can perform rotational and translational movements. As already described in the mathematical model of quadrotor drone (4.2), the rotational movements are independent of the translational ones, but the converse is not true. Therefore it is possible to implement two different types of synchronization: the first one controls only the attitude of the drone, without considering the translation movements, and the second one allows to modify at the same time the attitude and position of the drone.

The leader drone is described by the continuous time system:

$$\begin{cases} T := br(\omega_{L,4}^2 - \omega_{L,2}^2)\Omega_x + br(\omega_{L,3}^2 - \omega_{L,1}^2)\Omega_y + \\ \quad \gamma(-\omega_{L,1}^2 + \omega_{L,2}^2 - \omega_{L,3}^2 + \omega_{L,4}^2)\Omega_z, \\ \Omega_{L,r} := -\omega_{L,1} + \omega_{L,2} - \omega_{L,3} + \omega_{L,4}, \\ B_L := J_{\mathcal{R}}\Omega_{L,r}\Omega_z, \\ \dot{W} = D^{-1}([\hat{J}_q, W^2] + [B_L, W] - \dot{B}_L L + T)D^{-1}, \\ \dot{Z} = ZW, \end{cases} \quad (7.27)$$

where all the constants used have the values specified in (4.6). The follower drone is described by the continuous time system:

$$\begin{cases} \Omega_{F,r} := -\omega_{F,1} + \omega_{F,2} - \omega_{F,3} + \omega_{F,4}, \\ B_F := J_{\mathcal{R}}\Omega_{F,r}\Omega_z, \\ \dot{V} = D^{-1}([\hat{J}_q, V^2] + [B_F, V] - \dot{B}_F)D^{-1} + U, \\ \dot{X} = XV. \end{cases} \quad (7.28)$$

The leader system is described by the variables  $(Z, W) \in \text{SO}(3) \times \mathfrak{so}(3)$  and the follower system by  $(X, V) \in \text{SO}(3) \times \mathfrak{so}(3)$ , while the control signal generated by

the PID controller is denoted as  $U$ , and it is defined as follows:

$$\begin{cases} E(t) := \text{Log}(X(t)^{-1}Z(t)), \\ \mathcal{E}(t) := W(t) - V(t), \\ \Psi(t) := \int_0^t E(\tau) d\tau, \\ \mathbb{S}_F(t, X, V) = D^{-1}([\hat{J}_q, V^2] + [B_F, V] - \dot{B}_F)D^{-1}, \\ U_C(t) := \dot{W}(t) - \mathbb{S}_F(t, X, V), \\ U(t) := \kappa_P E(t) + \kappa_I \Psi(t) + \kappa_D \mathcal{E}(t) + U_C(t) \end{cases} \quad (7.29)$$

A discrete time systems of the leader, realized with a forward Euler method and used in the simulations, is the following:

$$\begin{cases} T_k := br(\omega_{L,4,k}^2 - \omega_{L,2,k}^2)\Omega_x + br(\omega_{L,3,k}^2 - \omega_{L,1,k}^2)\Omega_y + \\ \quad \gamma(-\omega_{L,1,k}^2 + \omega_{L,2,k}^2 - \omega_{L,3,k}^2 + \omega_{L,4,k}^2)\Omega_z, \\ \Omega_{L,r,k} := -\omega_{L,1,k} + \omega_{L,2,k} - \omega_{L,3,k} + \omega_{L,4,k}, \\ B_{L,k} := J_{\mathcal{R}}\Omega_{L,r,k}\Omega_z, \\ W_{k+1} = W_k + hD^{-1}([\hat{J}_q, W_k^2] + [B_{L,k}, W_k] - \frac{1}{h}(B_{L,k} - B_{L,k-1}) + T_k)D^{-1}, \\ Z_{k+1} = Z_k \text{Exp}(hW_k), \end{cases} \quad (7.30)$$

where  $B_{L,-1} = 0$ . Likewise, a discrete time systems of the follower is the following:

$$\begin{cases} \Omega_{F,r,k} := -\omega_{F,1,k} + \omega_{F,2,k} - \omega_{F,3,k} + \omega_{F,4,k}, \\ B_{F,k} := J_{\mathcal{R}}\Omega_{F,r,k}\Omega_z, \\ V_{k+1} = V_k + hD^{-1}([\hat{J}_q, V_k^2] + [B_{F,k}, V_k] - \frac{1}{h}(B_{F,k} - B_{F,k-1}))D^{-1} + hU_k, \\ X_{k+1} = X_k \text{Exp}(hV_k), \end{cases} \quad (7.31)$$

where  $B_{F,-1} = 0$ .

In the discrete time version, the leader system is described by the variables  $(Z_k, W_k) \in \text{SO}(3) \times \mathfrak{so}(3)$  and the follower system by  $(X_k, V_k) \in \text{SO}(3) \times \mathfrak{so}(3)$ , while the discrete time version of the control signal generated by the PID controller

is denoted as  $U_k$ , and it is defined as follows:

$$\begin{cases} E_k := \text{Log}(X_k^{-1}Z_k), \\ \mathcal{E}_k := W_k - V_k, \\ \Psi_k := h \sum_{i=0}^k E_i, \\ S_{F,k} := D^{-1}([\hat{f}_q, V_k^2] + [B_{F,k}, V_k] - \frac{1}{h}(B_{F,k} - B_{F,k-1}))D^{-1}, \\ U_{C,k} := \begin{cases} -S_F(0, X_0, V_0), & \text{if } k = 0, \\ \frac{1}{h}(W_k - W_{k-1}) - S_{F,k}, & \text{if } k > 0, \end{cases} \\ U_k := \kappa_P E_k + \kappa_I \Psi_k + \kappa_D \mathcal{E}_k + U_{C,k}, \end{cases} \quad (7.32)$$

where  $B_{F,-1} = 0$ .

## **7.7 Adaptation of an L-PID controller to the time-synchronization of the attitude and of the positioning of two quadrotor drones**

Before talking about joint attitude/position synchronization, it is necessary to make a note on the equations and the methodology used. In fact, in this case, unlike those previously seen, a purely mathematical procedure was not adopted to obtain the equations of the control signal, but instead a more empirical method was used, derived from observations and reasoning. The devised controller stems from a combination of one for the attitude, developed on the Lie group  $\text{SO}(3)$ , and one for the position, developed in  $\mathbb{R}^3$ . It is important to consider that, in the case of the drone, a position control is able to move it only along the direction perpendicular to the drone itself. Therefore, in this case, attitude control must not depend only on synchronization to the attitude of leader, but must also take into account the requirements of position control. For this reason, that is that the controller is made in a combined manner, the theorem seen for synchronization does not apply, therefore synchronization is not guaranteed for all cases. However, many simulations have been carried out and, by appropriately varying the coefficients, it has been seen that synchronization occurs in all cases.

To solve the problem of position control, we started from the hovering of the drone. Indeed, the four propellers speeds were obtained considering that the thrust

---

by the four motors balances perfectly the gravitational force. In particular, it was considered that the equation of acceleration is set to zero, so the effect of control balances the effects of the internal dynamics of the drone (gravitational force and aerodynamic drag). Since the drone does not move the aerodynamic drag is null, and being horizontal, the  $X$  attitude matrix becomes the identity, namely:

$$\frac{1}{2} \frac{b}{M_q} (\omega_1^2 + \omega_2^2 + \omega_3^2 + \omega_4^2) e_z = p e_z, \quad (7.33)$$

For the drone to move, it is instead necessary to apply an acceleration to the system (therefore a force), which does not cancel with the weight force, but produces instead a change in speed. It is important to remember that the thrust produced by the drone has direction that is perpendicular to the plane formed by the four fans, so if the drone is tilted away from the horizontal plane, the acceleration produced will not be uniquely along the  $z$  axis, but will also have components in the  $x - y$  plane. *Therefore, it is clear that to make the drone move in all directions of space it is also necessary to apply a rotation to steer the thrust of the propellers in the right direction.* The control action must satisfy the following equations:

$$\frac{1}{2} \frac{b}{M_q} (\omega_1^2 + \omega_2^2 + \omega_3^2 + \omega_4^2) X e_z = \alpha, \quad (7.34)$$

where  $X \in \text{SO}(3)$  is the follower attitude state, while  $\alpha$  is the control signal generated by the PID controller. Indeed, the acceleration generated by the drone is along the direction  $X e_z$ , while the acceleration required by the controller is along  $\alpha$ . Obviously, the PID controller does not take into consideration the physical feasibility of its own control signal, therefore the  $\alpha$  signal will generate a move that will not be along the direction perpendicular to the drone. So it is necessary to carry out a projection of the control signal along the direction perpendicular to the drone  $X e_z$ , which is the actual control that can be performed (that in physical terms is an acceleration in space  $\mathbb{R}^3$ , therefore an array of three elements). It is clear that if the  $\alpha$  signal gives an acceleration near the  $X e_z$  direction, the projection of this vector will be approximately equal to the original vector field  $\alpha$  generated by the controller, and therefore synchronization can take place. But if the PID gives an

acceleration in a direction nearly parallel to the plane formed by the fans of the propellers, its projection in the  $Xe_z$  direction is almost zero: in this case, position synchronization does not take place.

The PID position controller this time was made only in its complete form, including the  $u_C$  signal, that in  $\mathbb{R}^3$  case it was obtained in the following way:

$$\begin{cases} e(t) := z(t) - x(t), \text{ (Control error)} \\ \varepsilon(t) := \dot{e}(t) = \dot{z}(t) - \dot{x}(t), \text{ (Control error velocity)} \\ \psi(t) := \int_0^t e(\tau) d\tau, \text{ (Integrated control error)} \\ \alpha(t) := \kappa_P e(t) + \kappa_I \psi(t) + \kappa_D \varepsilon(t) + u_C(t), \text{ (Control field)} \end{cases} \quad (7.35)$$

where  $z(t) \in \mathbb{R}^3$  is a reference point, which may be moving over time, with  $u_C(t)$  to be defined. The controlled system, considering as control signal  $\alpha$  and not its projection, is:

$$\begin{cases} \dot{v} = \alpha - p e_z - \frac{1}{M_q} \Gamma v, \\ \dot{x} = v. \end{cases} \quad (7.36)$$

Taking the derivative of the error field  $\varepsilon$  and recalling the sub-model (7.36) leads to:

$$\dot{\varepsilon} = \ddot{z} - \dot{v} = \ddot{z} - \alpha + p e_z + \frac{1}{M_q} \Gamma v. \quad (7.37)$$

Plugging the equations (7.35) into the equation (7.37) yields

$$\dot{\varepsilon} = \ddot{z} + p e_z + \frac{1}{M_q} \Gamma v - \kappa_P e + \kappa_I \psi + \kappa_D \varepsilon + u_C. \quad (7.38)$$

The term  $u_C$  is meant to cancel all terms in the tight-hand side of the above expression that do not depend on the error-type fields, namely:

$$u_C := \ddot{z} + p e_z + \frac{1}{M_q} \Gamma v. \quad (7.39)$$

The resulting error dynamics is governed by the equation

$$\dot{\varepsilon} + \kappa_P e + \kappa_I \psi + \kappa_D \varepsilon = 0. \quad (7.40)$$

Instead, the synchronization of the attitude this time is more difficult than the previous case, where it had been taken independently. Indeed, the control signal

---

has to be divided in two parts: the first one must lead to synchronization to the attitude of the leader, while the second one must align the  $Xe_z$  direction of the follower with  $\alpha$  signal generated by the PID controller for the position. In this way, the projection of  $\alpha$  on the  $Xe_z$  direction is maximal and position synchronization can be achieved.

The first part of the controller was made in the same way of previous Section 7.6, and showed in the system (7.29), in its complete form, including the  $U_C$  signal, while the second part does not follow a precise method, but it was obtained empirically, through some important considerations. Thus, the PID function becomes:

$$\left\{ \begin{array}{l} m(t) := (X(t)e_z) \wedge \alpha(t) = \begin{bmatrix} m_x(t) & m_y(t) & m_z(t) \end{bmatrix}^\top, \\ M(t) := c \begin{bmatrix} 0 & -m_z(t) & m_y(t) \\ m_z(t) & 0 & -m_x(t) \\ -m_y(t) & m_x(t) & 0 \end{bmatrix}, \\ E(t) := \text{Log}(X(t)^{-1}Z(t)) + M(t), \\ \mathcal{E}(t) := W(t) - V(t) - \dot{M}(t), \\ \Psi(t) := \int_0^t E(\tau) d\tau, \\ \mathbb{S}_F(t, X, V) = D^{-1}([\hat{J}_q, V^2] + [B_F, V] - \dot{B}_F)D^{-1}, \\ U_C(t) := \dot{W}(t) - \mathbb{S}_F(t, X, V), \\ U(t) := \kappa_P E(t) + \kappa_I \Psi(t) + \kappa_D \mathcal{E}(t) + U_C(t) \end{array} \right. \quad (7.41)$$

where the symbol  $\wedge$  denotes a vector cross-product in  $\mathbb{R}^3$ , the constant  $c > 0$  represents the weight of the error  $M$  within the PID control signal, and the error  $M$  is defined as the skew-symmetric matrix obtained from the cross product of  $Xe_z$  and  $\alpha$ , as generated by the position controller. The result is a vector which indicates in which direction and of which angle the first vector must be rotated to obtain the second. The complete control field is therefore represented by  $U$ , showed in the system (7.41), and it can be seen that it produces an angular acceleration, because the result belongs to  $\mathfrak{so}(3)$ .

The complete continuous time systems representing the leader and follower, together with the control fields that afford the synchronization of two drones about

their position and attitude, are summarized in the following.

The leader drone is represented by the following system of differential equations:

$$\begin{cases} T := br(\omega_{L,4}^2 - \omega_{L,2}^2)\Omega_x + br(\omega_{L,3}^2 - \omega_{L,1}^2)\Omega_y + \gamma(-\omega_{L,1}^2 + \omega_{L,2}^2 - \omega_{L,3}^2 + \omega_{L,4}^2)\Omega_z, \\ \Omega_{L,r} := -\omega_{L,1} + \omega_{L,2} - \omega_{L,3} + \omega_{L,4}, \\ B_L := J_{\mathcal{R}}\Omega_{L,r}\Omega_z, \\ \dot{W} = D^{-1}([\hat{J}_q, W^2] + [B_L, W] - \dot{B}_L + T)D^{-1}, \\ \dot{Z} = ZW \\ \dot{w} = \frac{1}{2} \frac{b}{M_q} (\omega_{L,1}^2 + \omega_{L,2}^2 + \omega_{L,3}^2 + \omega_{L,4}^2) Ze_z - p e_z - \frac{1}{M_q} \Gamma w, \\ \dot{z} = w. \end{cases} \quad (7.42)$$

The controlled follower drone is represented by the following system of differential equations:

$$\begin{cases} \Omega_{F,r} := -\omega_{F,1} + \omega_{F,2} - \omega_{F,3} + \omega_{F,4}, \\ B_F := J_{\mathcal{R}}\Omega_{F,r}\Omega_z, \\ \dot{V} = D^{-1}([\hat{J}_q, V^2] + [B_F, V] - \dot{B}_F)D^{-1} + U, \\ \dot{X} = XV \\ \dot{v} = \alpha^\top (X e_z)(X e_z) - p e_z - \frac{1}{M_q} \Gamma v, \\ \dot{x} = v. \end{cases} \quad (7.43)$$

The leader system is described by the variables  $(Z, W) \in \text{SO}(3) \times \mathfrak{so}(3)$  for its attitude and  $(z, w) \in \mathbb{R}^3 \times \mathbb{R}^3$  for its position, while the follower system is described by  $(X, V) \in \text{SO}(3) \times \mathfrak{so}(3)$  for its attitude and  $(x, v) \in \mathbb{R}^3 \times \mathbb{R}^3$  for its position. While the control position signal generated by the first PID controller is denoted as  $\alpha$  and the control attitude signal generated by the second PID controller is denoted as  $U$ . Since the  $\alpha$  signal is not physically applicable, having a different direction from that of the thrust generated by the propellers, its projection long the rotated vertical axis  $X e_z$  is applied.

The discrete time systems to implement the leader drone and the follower drone, realized with the Euler method and used in the simulations, are expressed in the following.

---

The leader drone may be implemented by the equations:

$$\begin{cases} T_k := br(\omega_{L,4,k}^2 - \omega_{L,2,k}^2)\Omega_x + br(\omega_{L,3,k}^2 - \omega_{L,1,k}^2)\Omega_y + \gamma(-\omega_{L,1,k}^2 + \omega_{L,2,k}^2 - \omega_{L,3,k}^2 + \omega_{L,4,k}^2)\Omega_z, \\ \Omega_{L,r,k} := -\omega_{L,1,k} + \omega_{L,2,k} - \omega_{L,3,k} + \omega_{L,4,k}, \\ B_{L,k} := J_{\mathcal{R}}\Omega_{L,r,k}\Omega_z, \\ W_{k+1} = W_k + hD^{-1}([\hat{f}_q, W_k^2] + [B_{L,k}, W_k] - \frac{1}{h}(B_{L,k} - B_{L,k-1}) + T_k)D^{-1}, \\ Z_{k+1} = Z_k \text{Exp}(hW_k) \\ w_{k+1} = w_k + h\left(\frac{1}{2}\frac{b}{M_q}(\omega_{L,1,k}^2 + \omega_{L,2,k}^2 + \omega_{L,3,k}^2 + \omega_{L,4,k}^2)Z_k e_z - p e_z - \frac{1}{M_q}\Gamma w_k\right), \\ z_{k+1} = z_k + h w_k, \end{cases} \quad (7.44)$$

where  $B_{L,-1} = 0$ .

The controlled follower drone may be implemented by the equations:

$$\begin{cases} \Omega_{F,r,k} := -\omega_{F,1,k} + \omega_{F,2,k} - \omega_{F,3,k} + \omega_{F,4,k}, \\ B_{F,k} := J_{\mathcal{R}}\Omega_{F,r,k}\Omega_z, \\ V_{k+1} = V_k + hD^{-1}([\hat{f}_q, V_k^2] + [B_{F,k}, V_k] - \frac{1}{h}(B_{F,k} - B_{F,k-1}))D^{-1} + hU_k, \\ X_{k+1} = X_k \text{Exp}(hV_k) \\ v_{k+1} = v_k + h\left(\alpha_k^\top (X_k e_z)(X_k e_z) - p e_z - \frac{1}{M_q}\Gamma v_k\right), \\ x_{k+1} = x_k + h v_k, \end{cases} \quad (7.45)$$

where  $B_{F,-1} = 0$ .

In the discrete time instance, the leader system is described by the variables  $(Z_k, W_k) \in \text{SO}(3) \times \mathfrak{so}(3)$  for its attitude and  $(z_k, w_k) \in \mathbb{R}^3 \times \mathbb{R}^3$  for its position, and the follower system by  $(X_k, V_k) \in \text{SO}(3) \times \mathfrak{so}(3)$  for its attitude and  $(x_k, v_k) \in \mathbb{R}^3 \times \mathbb{R}^3$  for its position. The discrete time version of the control position signal generated by the first PID controller is denoted as  $\alpha_k$  and the discrete time version of the control attitude signal generated by the second PID controller is denoted as

$U_k$  and they are defined as

$$\begin{cases} e_k := z_k - x_k, \\ \varepsilon_k := w_k - v_k, \\ \Psi_k := h \sum_{i=0}^k e_i, \\ u_{C,k} := \begin{cases} p e_z + \frac{1}{M_q} \Gamma v_0, & \text{if } k = 0, \\ \frac{1}{h} (w_k - w_{k-1}) + p e_z + \frac{1}{M_q} \Gamma v_k, & \text{if } k > 0, \end{cases} \\ \alpha_k := \kappa_P e_k + \kappa_I w_k + \kappa_D \varepsilon_k + u_{C,k}, \end{cases} \quad (7.46)$$

for the translational component of motion, and by

$$\begin{cases} m_k := (X_k e_z) \wedge \alpha_k = \begin{bmatrix} m_{x,k} & m_{y,k} & m_{z,k} \end{bmatrix}^\top \\ M_k := c(m_{x,k} \Omega_x + m_{y,k} \Omega_y + m_{z,k} \Omega_z), \\ E_k := \text{Log}(X_k^{-1} Z_k) + M_k, \\ \mathcal{E}_k := W_k - V_k - \frac{1}{h} (M_k - M_{k-1}), \\ \Psi_k := \sum_{i=0}^k E_i h, \\ S_{F,k} := D^{-1} ([\hat{f}_q, V_k^2] + [B_{F,k}, V_k] - \frac{1}{h} (B_{F,k} - B_{F,k-1})) D^{-1}, \\ U_{C,k} := \begin{cases} -S_{F,0}, & \text{if } k = 0, \\ \frac{1}{h} (W_k - W_{k-1}) - S_{F,k}, & \text{if } k > 0, \end{cases} \\ U_k := \kappa_P E_k + \kappa_I \Psi_k + \kappa_D \mathcal{E}_k + U_{C,k}, \end{cases} \quad (7.47)$$

for the rotational component of motion, where  $B_{F,-1} = 0$ .

## 8. Numerical experiments on the time-synchronization of oscillators, satellites and drones

The present section illustrates L-PID-based synchronization of second-order dynamical systems taking as cases of study two Hard Duffing oscillators represented graphically as two ‘cubes’, two identical gyrostat satellites and two identical quadrotor drones. The case of Hard Duffing oscillator is used as ‘Toy Problem’ for subsequent simulations, that represent real cases. For the sake of clarity, the synchronization of the motion of two quadcopters is treated in two different ways: first, pure rotation synchronization is illustrated; second, mixed rotation/translation synchronization is discussed from a theoretical point of view and successively illustrated numerically, since this specific instance of synchronization requires to modify the control equations non-trivially.

In all experiments presented in this section, the stepsize was set to  $h = 0.001$ .

### 8.1 Synchronization of two cubes

In this subsection it will be treated the synchronization of two simple 3-dimensional and ideal objects, two cubes rotating with respect to the same point, that corresponds to their central point. The internal dynamics of the systems are described by two hard Duffing oscillators on the Lie-Group  $SO(3)$ , with different reference points.

The two cubes dimensions are the same and the initial state of the two bodies can be chosen as random matrices belonging to  $SO(3)$ . In the following simulations there are some cases of synchronization of the two cubes where the leader has its own dynamics, while the follower is controlled by the L-PID controller, described in the Section 7.2, whose aim is to reduce the error with respect to leader's state to zero.

In the first simulations the L-PID controller is not provided of the  $U_C$  term, but it is only composed by proportional, derivative and integral terms, while in the second simulations there is also the  $U_C$  term that is used to delete the internal dynamics of the follower in order to make synchronization quicker.

The reference attitudes of the two cubes can be chosen randomly, and they can be the same or different for the leader and follower.

It can be seen in Figure 8.1 that in the case in which there is not the  $U_C$  term, if the reference attitudes are different then synchronization is not achieved, while in the presence of  $U_C$  it is achieved, as confirmed by the Figure 8.2.

Instead, if the reference attitudes are the same for the leader and the follower, synchronization is achieved both in the case with  $U_C$  and without  $U_C$ . The Figure 8.3 illustrates the second case.

From the numerical simulations it can be seen that if the two cubes achieve synchronization and the distance figure between the follower's state and the leader's state tends to zero over time.

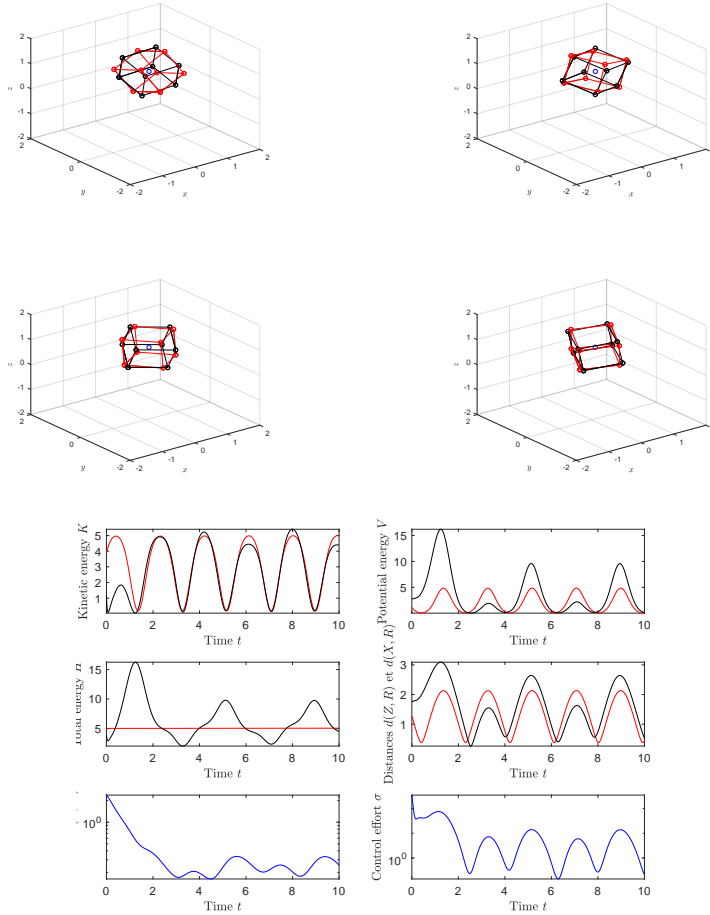


Figure 8.1: Synchronization of two cubes with different reference attitudes, where the follower is controlled by a L-PID controller, without the contribution of  $U_C$ . The first four figures represent four successive instants during the process of synchronization of the two bodies. In particular the black object denotes the follower, while the red one denotes the leader. The last six figures show the kinetic, potential and total energy of the follower and leader, the behavior of the distance between the leader and follower attitude, the distance between the leader and its reference attitude and the distance between the follower and its reference attitude, and the control effort  $\sigma$ . In the attitude controller the coefficients are  $\kappa_P = 10$ ,  $\kappa_I = 5$ ,  $\kappa_D = 10$ .

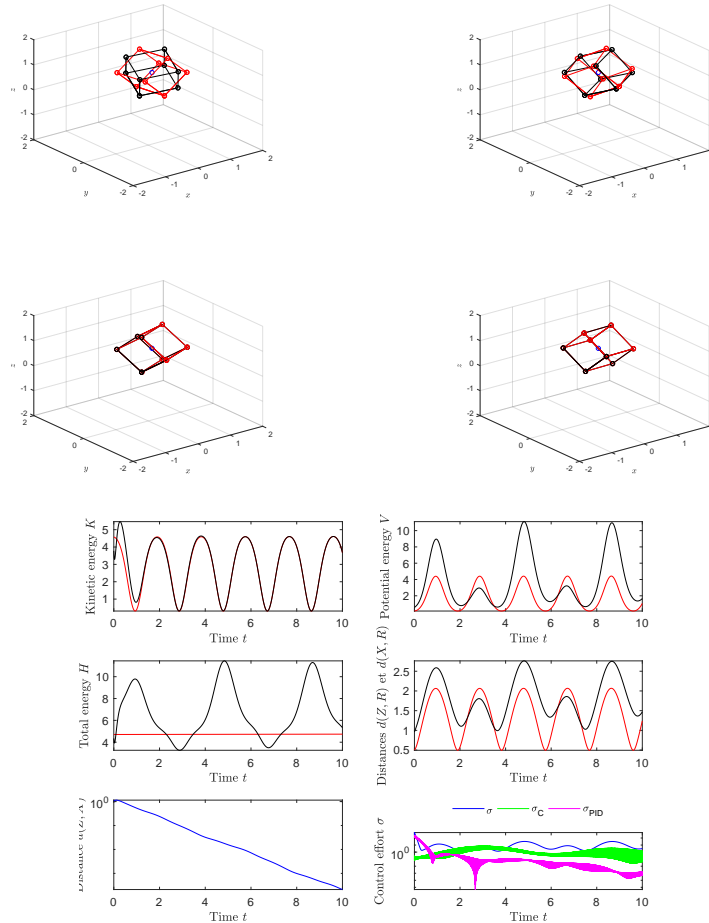


Figure 8.2: Synchronization of two cubes with different reference attitudes, where the follower is controlled by a L-PID controller. The first four figures represent four successive instants during the process of synchronization of the two bodies. In particular the black object denotes the follower, while the red one denotes the leader. The last six figures show the kinetic, potential and total energy of the follower and leader, the behavior of the distance between the leader and follower attitude, the distance between the leader and its reference attitude and the distance between the follower and its reference attitude, and the three control efforts:  $\sigma$ ,  $\sigma_C$  and  $\sigma_{PID}$ . In the attitude controller the coefficients are  $\kappa_P = 10$ ,  $\kappa_I = 5$ ,  $\kappa_D = 10$ .

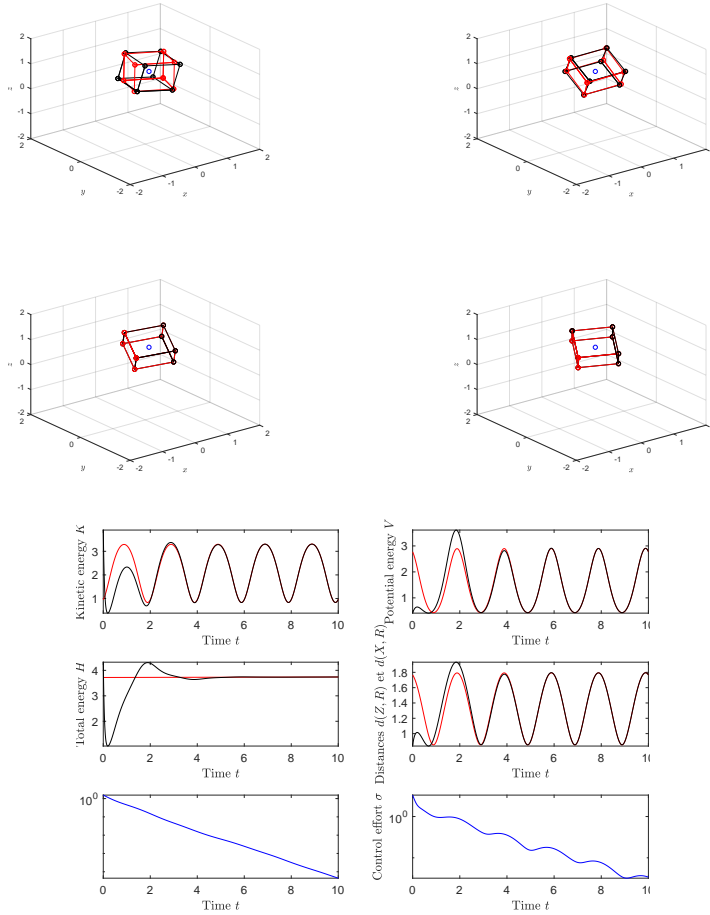


Figure 8.3: Synchronization of two cubes with same reference attitudes, where the follower is controlled by a L-PID controller, without the contribution of  $U_C$ . The first four figures represent four successive instants during the process of synchronization of the two bodies. In particular the black object denotes the follower, while the red one denotes the leader. The last six figures show the kinetic, potential and total energy of the follower and leader, the behavior of the distance between the leader and follower attitude, the distance between the leader and its reference attitude and the distance between the follower and its reference attitude, and the control effort  $\sigma$ . In the attitude controller the coefficients are  $\kappa_P = 10$ ,  $\kappa_I = 5$ ,  $\kappa_D = 10$ .

## **8.2 Gyrostat satellites synchronization**

Several simulations have been made to verify the efficacy of the L-PID regulation theory. In particular, one of the main differences was seen if the control signal  $U_C$  is used or not, because it is able to cancel the internal dynamics of the follower and compensate for the acceleration difference of the two systems. It is possible to see that the synchronization is performed in a better way if  $U_C$  is applied. When  $U_C$  is not applied (Figure 8.4), all the contribution of the control signal is given by the pure PID component. The control effort can never decrease, since the two gyrostats have different internal dynamics: this implies that, even once they have reached the same attitude, they will not follow the same trajectory, and therefore the controller must continually modify the follower attitude without being able to weaken its action. Moreover, it should be noted that without the term  $U_C$ , the Theorem 7.2.1 loses its validity, and therefore the synchronization operation is not guaranteed in any case. Instead, synchronization is guaranteed if  $U_C$  is applied. In particular, Theorem 7.2.1 guarantees this, and further demonstrates that it is not necessary for the controller to be a PID, but it is sufficient that the proportional and one of the integral or derivative action is carried out.

In the simulations, several tests have been carried out, both to demonstrate the effective validity of the theorem and to see the contribution of each of the three parts that make up the PID controller.

First, we tried to apply a PID without an integral nor a derivative component, so that only the proportional control term is present, and it was verified that the error does not converge to zero, as can be seen in Figure 8.5. The error behaves in a similar manner if a control action is applied which does not contain the proportional control component, but only integral and derivative, as can be seen in the Figure 8.6. This happens precisely because in these two cases the conditions of the Theorem 7.2.1 are not respected. The synchronization could happen in some particular cases, even if the theorem is not respected, in which the initial states of attitude of the two gyrostats ( $Z \in SO(3)$  in the leader case and  $X \in SO(3)$  in

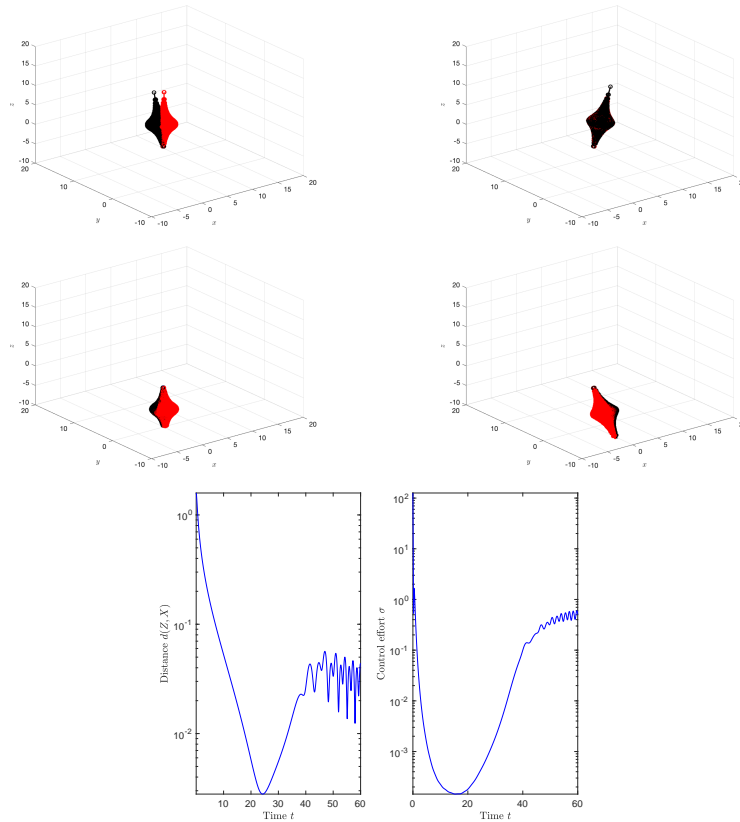


Figure 8.4: Synchronization of two gyrostat satellites, where the follower is controlled by a L-PID controller, without the contribution of  $U_C$ . The first four figures represent four successive instants during the process of synchronization of the two bodies. In particular the black object denotes the follower, while the red one denotes the leader. The last two figures show the behavior of the distance between the leader and follower attitude and the control effort  $\sigma$ . The proportional control coefficient was set to  $\kappa_P = 10$ , the integral control coefficient was set to  $\kappa_I = 5$  and the derivative coefficient was set to  $\kappa_D = 10$ .

the follower case) are very close, but it should be guaranteed in every case.

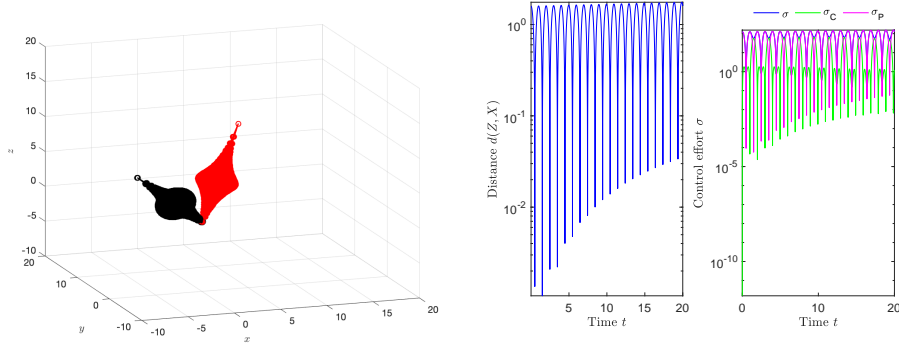


Figure 8.5: Synchronization of two gyrostat satellites, where the follower is controlled by a L-PID controller and the PID is made by only the proportional part (P). The first figure represents the last instant of the process of synchronization of the two bodies. In particular the black object denotes the follower, while the red one denotes the leader. The last two figures show the behavior of the distance between the leader and follower attitude and the three control efforts:  $\sigma$ ,  $\sigma_C$  and  $\sigma_P$ . The proportional control coefficient was set to  $\kappa_P = 10$ , the integral control coefficient was set to  $\kappa_I = 0$  and the derivative coefficient was set to  $\kappa_D = 0$ .

Otherwise, synchronization is successful if Theorem 7.2.1 is respected, and therefore when the control action is of type PI (proportional-integral), PD (proportional-derivative) or PID (proportional-integral-derivative). In particular, it was noted how the three coefficients of the actions of the PID ( $\kappa_P$ ,  $\kappa_I$ ,  $\kappa_D$ ) affect final synchronization. In fact it is important to note that although the PID is implemented on a curved Lie group, the error system is linear and therefore the whole theory of control of linear systems can be applied, as showed in the Section 7.1. As verified in the simulations, the three coefficients have very specific properties. In particular the coefficient  $\kappa_P$  is responsible for the proportional action: the higher the value, the faster the synchronization, because a higher value of this parameter entails a greater reactivity of the system and a shorter rise time, similarly to linear systems. Otherwise, a high  $\kappa_D$  value, which is applied to the derivative action, worsens the reactivity of the system, but improves its stability and makes the system exhibit much less oscillations before achieving a permanent regime. In fact, it can be

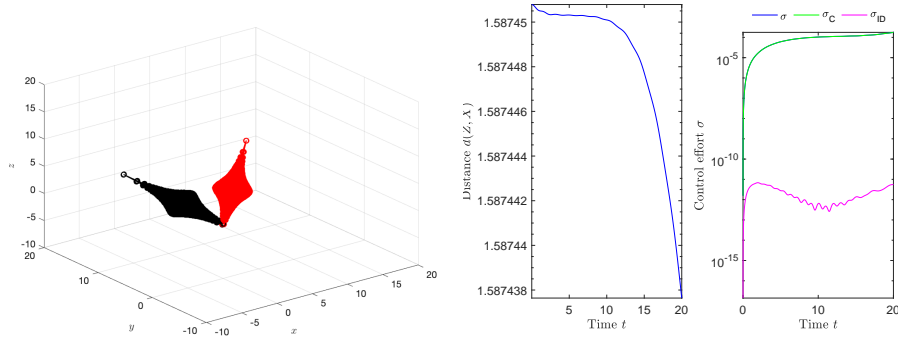


Figure 8.6: Synchronization of two gyrostatt satellites, where the follower is controlled by a L-PID controller and the PID is made by only the integral and derivative parts (ID). The first figure represents the last instant of the process of synchronization of the two bodies. In particular the black object denotes the follower, while the red one denotes the leader. The last two figures show the behavior of the distance between the leader and follower attitude and the three control efforts:  $\sigma$ ,  $\sigma_C$  and  $\sigma_{ID}$ . The proportional control coefficient was set to  $\kappa_P = 0$ , the integral control coefficient was set to  $\kappa_I = 5$  and the derivative coefficient was set to  $\kappa_D = 10$ .

noted that in the simulation in which the controller is of the PI type (so the derivative action is not applied, and  $\kappa_D = 0$ ), the follower state oscillates much around the leader system state, even if it achieves synchronization, as confirmed by the Figure 8.7. In fact, from the distance graph it is possible to see that it oscillates, but with very small orders of magnitude. Finally, a higher value of the last coefficient, that is  $\kappa_I$ , guarantees to have an ever-smaller error at a permanent regime, but worsening the stability of the system. Indeed in Figure 8.8, where integral control is not applied, it is possible to see that the error tends to zero at the beginning, but then increases again, however remaining very small and allowing synchronization. It is important, therefore, to be able to find a compromise between the effects of each action, by appropriately varying the value of the three coefficients based on the control specifications. So the controller is implemented in its complete form (proportional, derivative and integral parts with the contribution of  $U_C$  are applied), as shown in the Figure 8.9, achieving the synchronization of the two systems.

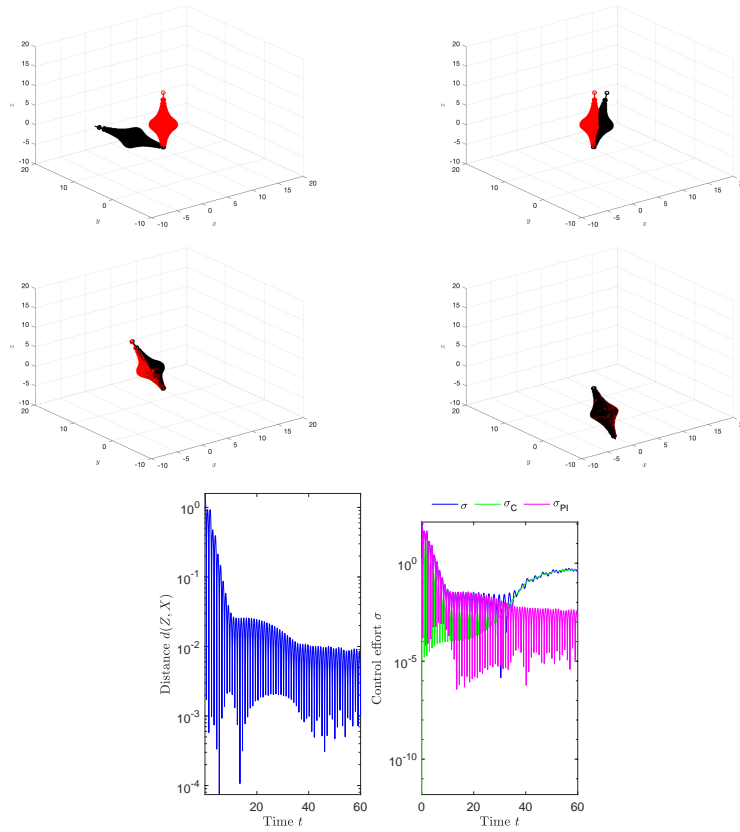


Figure 8.7: Synchronization of two gyrostatt satellites, where the follower is controlled by a L-PID controller and the PID is made by only proportional and integral parts (PI). The first four figures represent four successive instants during the process of synchronization of the two bodies. In particular the black object denotes the follower, while the red one denotes the leader. The last two figures show the behavior of the distance between the leader and follower attitude and the three control efforts:  $\sigma$ ,  $\sigma_C$  and  $\sigma_{PI}$ . The proportional control coefficient was set to  $\kappa_P = 10$ , the integral control coefficient was set to  $\kappa_I = 5$  and the derivative coefficient was set to  $\kappa_D = 0$ .

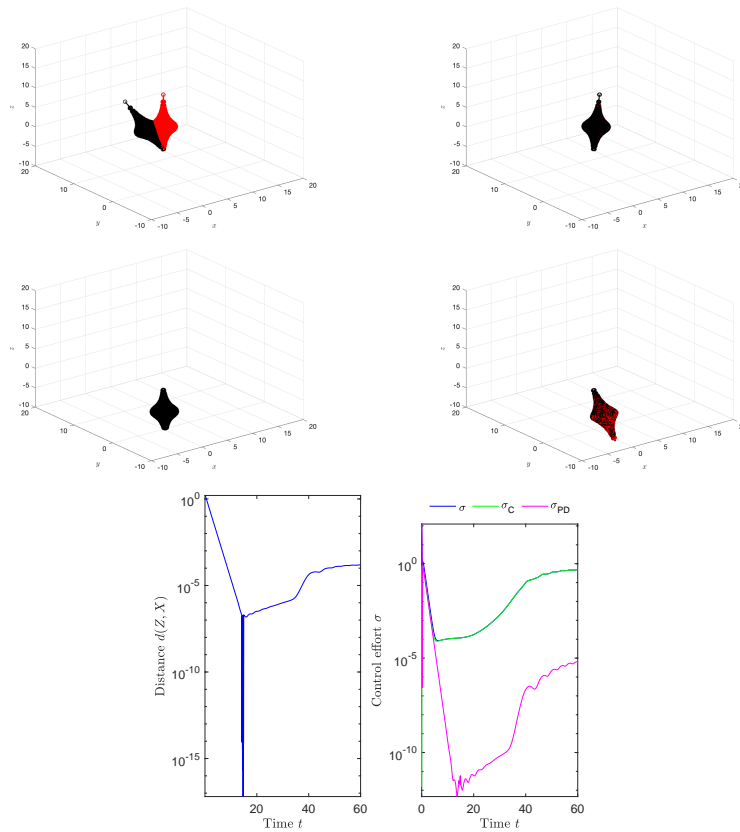


Figure 8.8: Synchronization of two gyrostatt satellites, where the follower is controlled by a L-PID controller and the PID is made by only proportional and derivative parts (PD). The first four figures represent four successive instants during the process of synchronization of the two bodies. In particular the black object denotes the follower, while the red one denotes the leader. The last two figures show the behavior of the distance between the leader and follower attitude and the three control efforts:  $\sigma$ ,  $\sigma_C$  and  $\sigma_{PD}$ . The proportional control coefficient was set to  $\kappa_P = 10$ , the integral control coefficient was set to  $\kappa_I = 0$  and the derivative coefficient was set to  $\kappa_D = 10$ .

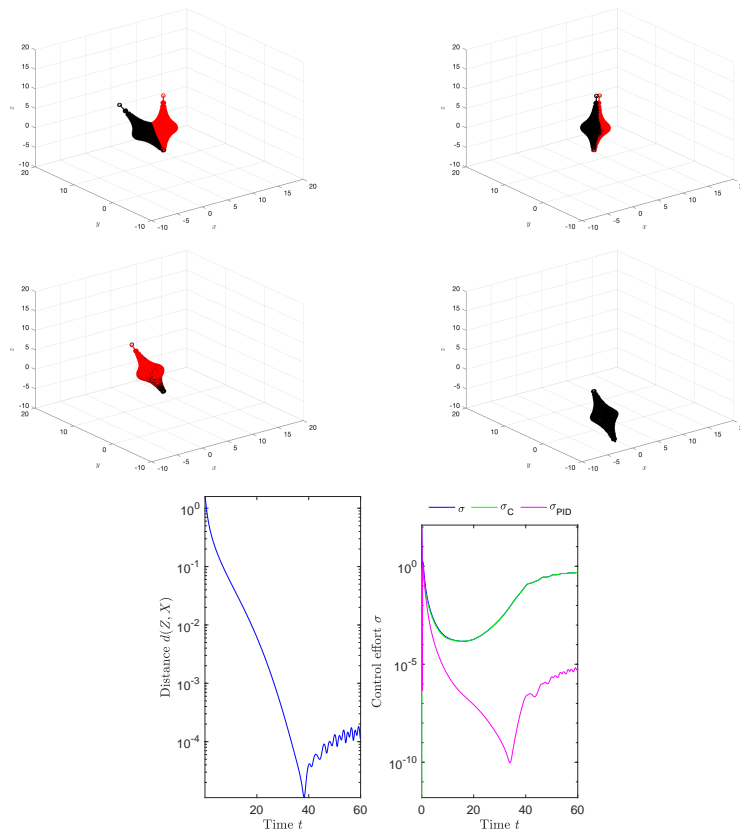


Figure 8.9: Synchronization of two gyrostat satellites, where the follower is controlled by a L-PID controller. The first four figures represent four successive instants during the process of synchronization of the two bodies. In particular the black object denotes the follower, while the red one denotes the leader. The last two figures show the behavior of the distance between the leader and follower attitude and the three control efforts:  $\sigma$ ,  $\sigma_C$  and  $\sigma_{PID}$ . The proportional control coefficient was set to  $\kappa_P = 10$ , the integral control coefficient was set to  $\kappa_I = 5$  and the derivative coefficient was set to  $\kappa_D = 10$ .

---

### 8.3 Quadrotor drones synchronization – attitude control

During the simulations, no differences were observed whether the control signal  $U_C$  is present or absent. Indeed, in this case, since the internal dynamics of the two drones are the same, once that synchronization is reached, therefore the leader and the follower systems reached the same attitude, they will begin to follow the same trajectory, making sure that the control field tends to zero. The purpose of term  $U_C$  is to cancel the internal dynamics of the follower, replacing it with that given by the leader, and compensate for the acceleration difference of the two systems. But since the two internal dynamics are the same, once the two drones have reached the same attitude, the contribution of the term  $U_C$  becomes dispensable. In particular, in the simulation where  $U_C$  is not applied, shown in Figure 8.10, synchronization is achieved. Indeed, it is possible to see that the  $U_C$  signal has a great value only at the beginning (if it is applied), when the two drones are not synchronized, but once they have reached the same attitude it vanishes to zero.

In the simulations, several tests have been carried out, both to demonstrate the effective validity of the theorem and to oversee the contribution of each of the three terms that make up the PID control field.

First, a PID controller comprising only a proportional control term was tested. The result of this test is that the distance between the leader's and the follower's states does not converge to zero, as can be seen in Figure 8.11. The error behaves in a similar manner if a control action is applied which does not contain the proportional part, but only integrative and derivative, as can be seen in the Figure 8.12. This happens because in these two cases the conditions of the Theorem 7.2.1 are not respected. Otherwise, synchronization is successful if Theorem 7.2.1 is respected, and therefore when the control action is of type PI (proportional-integral), PD (proportional-derivative) or PID (proportional-integral-derivative). It can be noted that in the simulation in which the controller is of the PI type (so the derivative action is not applied, and  $\kappa_D = 0$ ), the follower state oscillates much around the leader system state, even if it achieves synchronization, as confirmed by the

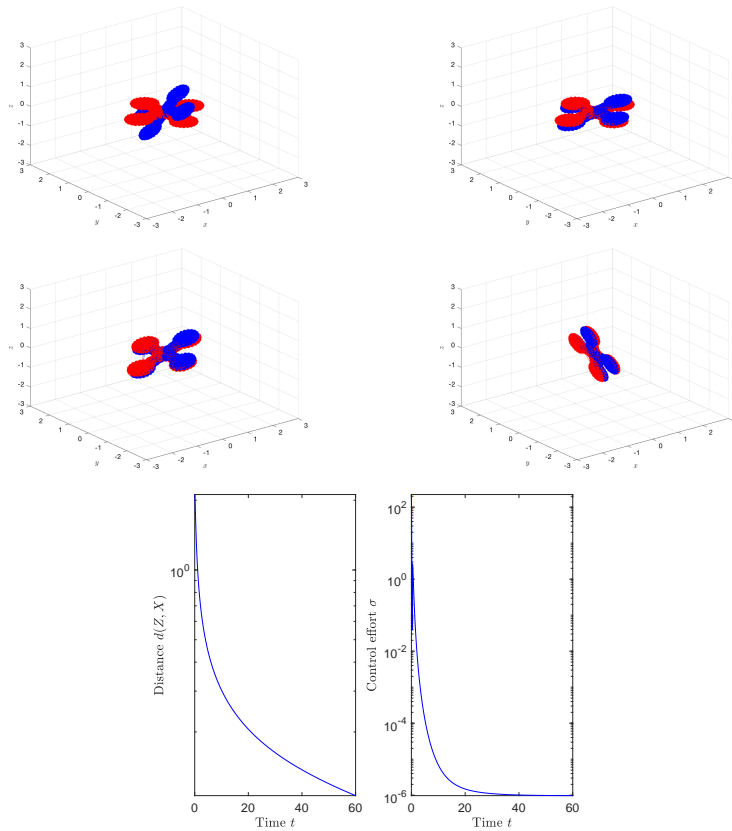


Figure 8.10: Synchronization of two drones, where the follower is controlled by a L-PID controller, without the contribution of  $U_C$ . The first four figures represent four successive instants during the process of synchronization of the two bodies. In particular the blue object denotes the follower, while the red one denotes the leader. The last two figures show the behavior of the distance between the leader and follower attitude and the control effort  $\sigma$ . The proportional control coefficient was set to  $\kappa_P = 10$ , the integral control coefficient was set to  $\kappa_I = 5$  and the derivative coefficient was set to  $\kappa_D = 10$ .

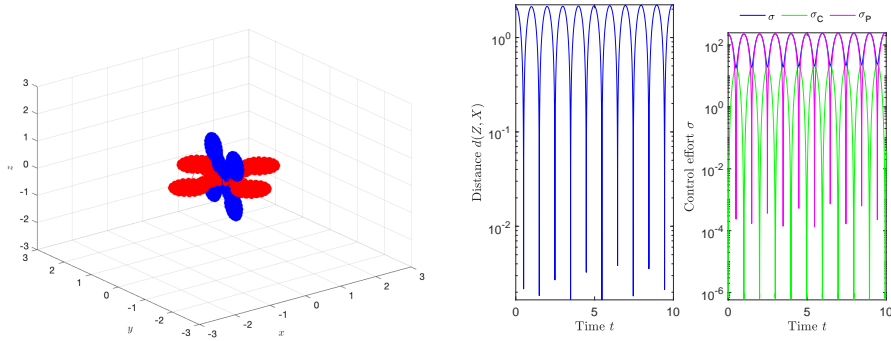


Figure 8.11: Synchronization of two drones, where the follower is controlled by a L-PID controller and the PID is made by only the proportional part (P). The first figure represents the last instant of the process of synchronization of the two bodies. In particular the blue object denotes the follower, while the red one denotes the leader. The last two figures show the behavior of the distance between the leader and follower attitude and the three control efforts:  $\sigma$ ,  $\sigma_C$  and  $\sigma_P$ . The proportional control coefficient was set to  $\kappa_P = 10$ , the integral control coefficient was set to  $\kappa_I = 0$  and the derivative coefficient was set to  $\kappa_D = 0$ .

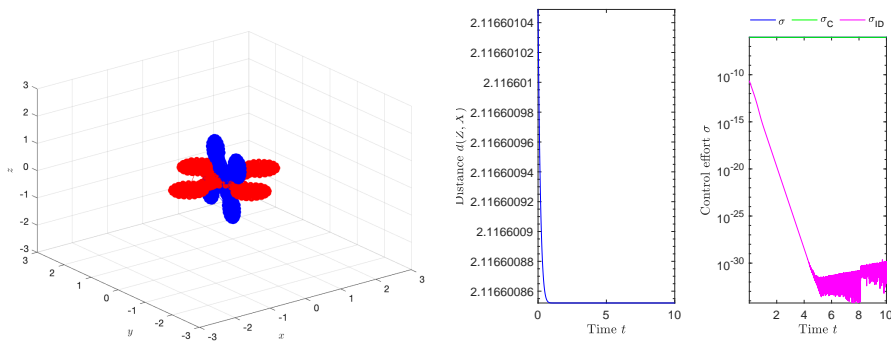


Figure 8.12: Synchronization of two drones, where the follower is controlled by a L-PID controller and the PID is made by only the integral and derivative parts (ID). The first figure represents the last instant of the process of synchronization of the two bodies. In particular the blue object denotes the follower, while the red one denotes the leader. The last two figures show the behavior of the distance between the leader and follower attitude and the three control efforts:  $\sigma$ ,  $\sigma_C$  and  $\sigma_{ID}$ . The proportional control coefficient was set to  $\kappa_P = 0$ , the integral control coefficient was set to  $\kappa_I = 5$  and the derivative coefficient was set to  $\kappa_D = 10$ .

Figure 8.13. Indeed, from the distance graph it is possible to see that it oscillates, but with very small orders of magnitude. Moreover the controller has been implemented in its complete form (proportional, derivative and integral parts with the contribution of  $U_C$  are applied), achieving the synchronization, as shown in the Figure 8.14.

In all numerical simulations where synchronization happens successfully, the values taken by the control efforts span several magnitude orders.

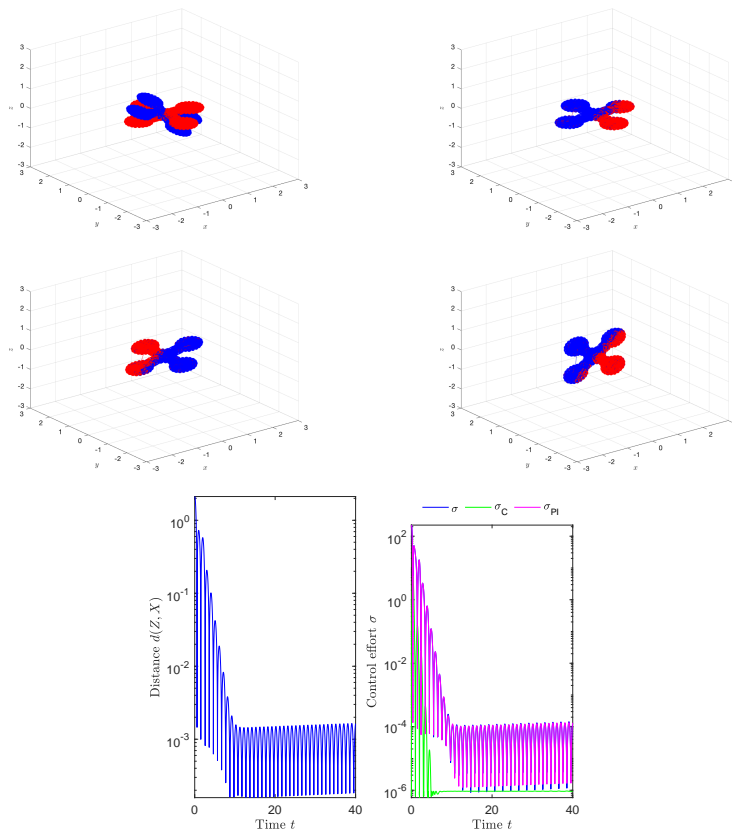


Figure 8.13: Synchronization of two drones, where the follower is controlled by a L-PID controller and the PID is made by only proportional and integral parts (PI). The first four figures represent four successive instants during the process of synchronization of the two bodies. In particular the blue object denotes the follower, while the red one denotes the leader. The last two figures show the behavior of the distance between the leader and follower attitude and the three control efforts:  $\sigma$ ,  $\sigma_C$  and  $\sigma_{PI}$ . The proportional control coefficient was set to  $\kappa_P = 10$ , the integral control coefficient was set to  $\kappa_I = 5$  and the derivative coefficient was set to  $\kappa_D = 0$ .

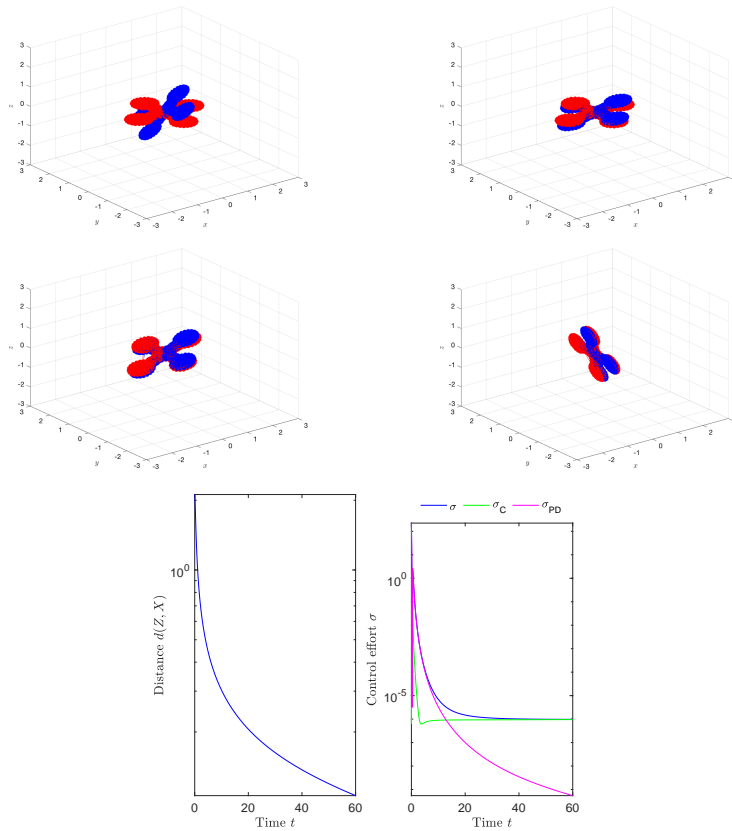


Figure 8.14: Synchronization of two drones, where the follower is controlled by a L-PID controller. The first four figures represent four successive instants during the process of synchronization of the two bodies. In particular the blue object denotes the follower, while the red one denotes the leader. The last two figures show the behavior of the distance between the leader and follower attitude and the three control efforts:  $\sigma$ ,  $\sigma_C$  and  $\sigma_{PID}$ . The proportional control coefficient was set to  $\kappa_P = 10$ , the integral control coefficient was set to  $\kappa_I = 5$  and the derivative coefficient was set to  $\kappa_D = 10$ .

---

## 8.4 Quadrotor drones synchronization – mixed attitude and position control

In the first numerical experiment, the synchronization/control goal is to drive the follower drone to take the same attitude as the leader drone, though the follower drone must sync to the position of the leader drone up to a fixed distance of 5 units along the  $z$  axis of the earth reference system.

In this case, the second part of the attitude controller (that depends on the error field  $M$ ) has a greater effect at the beginning of the synchronization, when the two drones must approach one another, then its contribution will become very small, since the direction perpendicular to the plane of the propellers and the direction of  $\alpha$  will almost coincide and it will no longer be necessary to apply any rotation to the follower drone to approach it to the leader. While the first part (that depends to the distance between the attitude states of the leader and the follower) has a smaller effect at the beginning, allowing the two drones to approach one another, then when they come sufficiently near, so the error field  $M$  will be very small, the rotation of the follower drone is determined almost exclusively by synchronization with the leader attitude.

In the first simulation, the leader makes only the maneuver “Yaw & Pitch (+ $x$ )” and synchronization is successful, as it can be observed from the results displayed in the Figure 8.15. It is interesting to note that by increasing the weight of  $M$  in the attitude controller, the range, where the distance between the two drones oscillates, decreases. However, at the same time the distance of the attitude between the two drones increases. So it is necessary to find a compromise between the two situations, finding the right values for the PID coefficients and weight of  $M$ , making sure that both synchronizations take place.

In the second numerical experiment, the leader makes three different maneuvers: “Pitch (+ $x$ ) & Roll (+ $y$ )”, “Yaw & Pitch (+ $x$ )” and “Yaw & Roll (– $y$ )”, creating a more complex maneuver in the space, and therefore more difficult to synchronize. From the Figure 8.16, it is possible to see that each time it changes

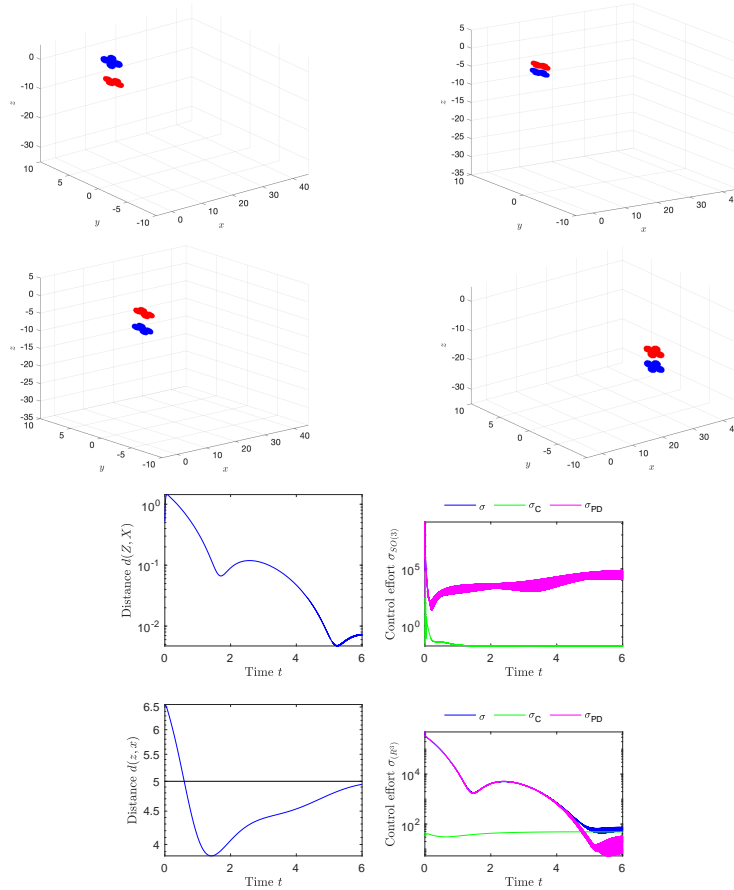


Figure 8.15: Synchronization of two drones, where the follower is controlled by a mixed attitude and position controller. The first four figures represent four successive instants during the process of synchronization of the two bodies. In particular the blue object denotes the follower, while the red one denotes the leader. The last four figures show the behavior of the distance between the leader and follower attitude, the distance between the leader and follower position, and the three control efforts of both control signal (position and attitude):  $\sigma$ ,  $\sigma_C$  and  $\sigma_{PID}$ . In the position controller the coefficients are  $\kappa_P = 100$ ,  $\kappa_I = 10$ ,  $\kappa_D = 80$ , while in the attitude controller the coefficients are  $\kappa_P = 50$ ,  $\kappa_I = 10$ ,  $\kappa_D = 50$ .

---

maneuver, the follower moves away. Therefore the distance between the two attitudes increases because the rotational effect to align the drone to the  $\alpha$  direction increases, losing synchronization with the leader. Thus, it is important that a sufficiently long time has elapsed since the last maneuver changes to properly achieve synchronization. In fact, from the simulations, it emerged that if the previous consideration is respected, the synchronization takes place in all cases.

From the simulations are emerged different considerations on the parameters of the two PID controllers. As already seen in the previous cases, by varying the coefficients of the PID improves the control obtained. In the case of mixed maneuvers, it is necessary to have the system very reactive, since the follower must be able to quickly change his trajectory when the leader changes maneuver. This thing, however, means that the system loses stability, not by synchronizing and seeing the follower “flying” around the leader. Finally, a higher value of the last coefficient, that is  $\kappa_I$ , guarantees to have an ever smaller error at a permanent regime, but worsening the stability of the system.

The orders of magnitude of the coefficients of two PID are related because the PID implemented on a Lie group uses the control signal of the PID implemented in  $\mathbb{R}^3$ . If the weight of the latter is too large, the rotation control will cause the  $\alpha$  signal is applied with its maximum value, rotating the drone towards the alpha direction, losing synchronization of the attitude with the leader. Therefore it is important that the follower is reactive to be able to follow all the movements and maneuvers that the leader performs, but it is still necessary to find a compromise in order not to make the system unstable.

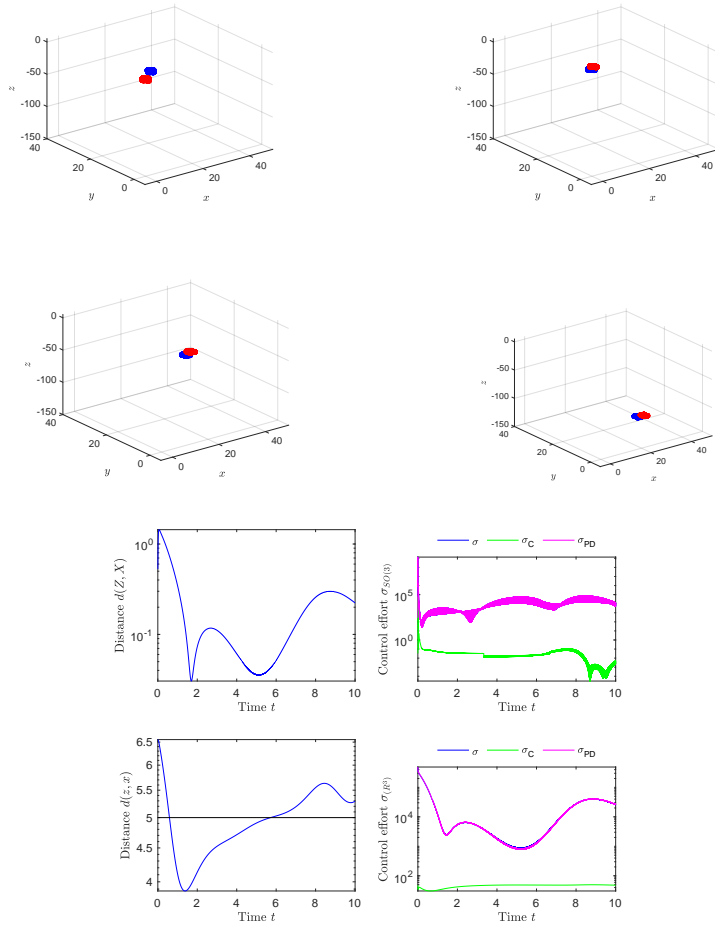


Figure 8.16: Synchronization of two drones, where the follower is controlled by mixed attitude and position controller and the leader performs three different maneuvers over the time. The first four figures represent four successive instants during the process of synchronization of the two bodies. In particular the blue object denotes the follower, while the red one denotes the leader. The last four figures show the behavior of the distance between the leader and follower attitude, the distance between the leader and follower position, and the three control efforts of both control signal (position and attitude):  $\sigma$ ,  $\sigma_C$  and  $\sigma_{PID}$ . In the position controller the coefficients are  $\kappa_P = 100$ ,  $\kappa_I = 10$ ,  $\kappa_D = 80$ , while in the attitude controller the coefficients are  $\kappa_P = 50$ ,  $\kappa_I = 10$ ,  $\kappa_D = 50$ .

## 9. Conclusion

Feedback control of dynamical systems on curved spaces in a synchronization new and interesting research field which poses some challenging design problems. An extension of the classical proportional-integral-derivative error-feedback control scheme to Lie-group-type systems, as proposed here, is an important achievement *per se*, which, in addition, carries along a number of noticeable results, such as the Theorem 7.2.1, that shed new lights on the application of a Lyapunov-type asymptotic stability theory to characterize an *ad hoc* Lie-algebra-type error dynamics for the closed loop system.

Such an extension was applied to achieve time-synchronization of the rotational component of rigid bodies motion, as exemplified by a number of numerical simulations carried out through the mathematical models of a gyrostat satellite and of a quad-rotor drone. As a by-product, a Lie-algebra-type sub-control scheme was proposed (through an empirical reasoning) and tested to achieve time-synchronization of the translational component of motion of a flying quadrotor drone.

I believe that the research endeavor summarized in the present document brings incremental knowledge in the mathematical understanding of non-linear control theory and that the in-depth analysis traced within this document paves the way to new and unexpected applications of manifold calculus.

# Acknowledgments

The present research work was completed while the author CM was taking an internship at the Agency for Science, Technology and Research (A\*STAR, Republic of Singapore) during April-June 2019. The author wishes to gratefully thank Dr. Hwee Kuan Lee who made this internship possible. The present research was advanced while the supervisor SF was on a temporary leave at the BII-A\*STAR institute, during May 2019, partially supported by the institute.

# Bibliography

- [1] D. ATHERTON, *Almost six decades in control engineering*, IEEE Control Systems Magazine, 34 (2014), pp. 103–110.
- [2] M. BECKER, R. SAMPAIO, S. BOUABDALLAH, V. DE PERROT, AND R. SIEGWART, *In-flight collision avoidance controller based only on os4 embedded sensors*, Journal of the Brazilian Society of Mechanical Sciences and Engineering, 34 (2012), pp. 294–307.
- [3] Z. BENIĆ, P. PILJEK, AND D. KOTARSKI, *Mathematical modelling of unmanned aerial vehicles with four rotors*, Interdisciplinary Description of Complex Systems, 14 (2016), pp. 88–100.
- [4] M. EIE AND S.-T. MINKING, *A Course on Abstract Algebra*, World Scientific, 2010.
- [5] S. FIORI, *Nonlinear damped oscillators on Riemannian manifolds: Fundamentals*, Journal of Systems Science and Complexity, 29 (2016), pp. 22–40.
- [6] ———, *Nonlinear damped oscillators on Riemannian manifolds: Numerical simulation*, Communications in Nonlinear Science and Numerical Simulation, 47 (2017), pp. 207–222.
- [7] ———, *Non-delayed synchronization of non-autonomous dynamical systems on Riemannian manifolds and its applications*, Nonlinear Dynamics, 94 (2018), pp. 3077–3100.

- [8] M. FÜGGER, T. NOWAK, AND B. CHARRON-BOST, *Diffusive clock synchronization in highly dynamic networks*, in 2015 49th Annual Conference on Information Sciences and Systems (CISS), March 2015, pp. 1–6.
- [9] Z.-M. GE AND T.-N. LIN, *Chaos, chaos control and synchronization of a gyrostat system*, Journal of Sound and Vibration, 251 (2002), pp. 519–542.
- [10] C. HALL, *Momentum transfer in two-rotor gyrostats*, Journal of Guidance, Control, and Dynamics, 19 (1996), pp. 1157–1161.
- [11] I. KOVACIC AND M. BRENNAN, *The Duffing Equation: Nonlinear Oscillators and their Behaviour*, Wiley, 2011.
- [12] M. KRSTIC, *On the applicability of PID control to nonlinear second-order systems*, National Science Review, 4 (2017), pp. 668–668.
- [13] M. MAGDY AND T. NG, *Regulation and control effort in self-tuning controllers*, IEE Proceedings D – Control Theory and Applications, 133 (1986), pp. 289–292.
- [14] J. MEI, M. JIANG, W. XU, AND B. WANG, *Finite-time synchronization control of complex dynamical networks with time delay*, Communications in Nonlinear Science and Numerical Simulation, 18 (2013), pp. 2462 – 2478.
- [15] K. OJO, S. OGUNJO, AND A. OLAGUNDOYE, *Projective synchronization via active control of identical chaotic oscillators with parametric and external excitation*, International Journal of Nonlinear Science, 24 (2017), pp. 76–83.
- [16] V. SARYCHEV, S. MIRER, AND A. DEGTYAREV, *The dynamics of a satellite-gyrostat with a single nonzero component of the vector of gyrostatic moment*, Cosmic Research, 43 (2005), pp. 268–279.
- [17] N. SHERIF AND E. MORSY, *Computing real logarithm of a real matrix*, International Journal of Algebra, 2 (2008), pp. 131–142.

- 
- [18] S. TAHIR, *The synchronization of identical memristors systems via Lyapunov direct method*, Applied and Computational Mathematics, 2 (2013), pp. 130–136.
- [19] C. TONG, *Lord Kelvin’s gyrostat and its analogs in physics, including the Lorenz model*, American Journal of Physics, 77 (2009), p. 526.
- [20] A. TYAGI AND J. DAVIS, *A recursive filter for linear systems on Riemannian manifolds*, in 2008 IEEE Conference on Computer Vision and Pattern Recognition, June 2008, pp. 1–8.
- [21] J. WU, Y. BAI, AND L. ZHANG, *Distributed time synchronization in wireless sensor networks via second-order consensus algorithms*, Transactions of Tianjin University, 21 (2015), pp. 113–121.
- [22] X. XI, S. MOBAYEN, H. REN, AND S. JAFARI, *Robust finite-time synchronization of a class of chaotic systems via adaptive global sliding mode control*, Journal of Vibration and Control, 24 (2018), pp. 3842–3854.
- [23] S. ZHU, *Analysis of spacecraft attitude control*, Master’s thesis, Lehigh University, 27 Memorial Drive West, Bethlehem, PA 18015, USA, 2016.